Stiffness measurements of thin and narrow superconducting rings

Tabo Omri

Stiffness measurements of thin and narrow superconducting rings

Research Thesis

Submitted in partial fulfillment of the requirements
for the degree of Master of Science in Physics

Tabo Omri

Submitted to the Senate
of the Technion — Israel Institute of Technology
Av 5786 Haifa August 2026

The thesis was done in the Faculty of Physics under the supervision of Prof. Keren Amit. The author of this thesis states that the research, including the collection, processing and presentation of data, addressing and comparing to previous research, etc., was done entirely in an honest way, as expected from scientific research that is conducted according to the ethical standards of the academic world. Also, reporting the research and its results in this thesis was done in an honest and complete manner, according to the same standards.

The Technion's funding of this research is hereby acknowledged.

Contents

List of Figures

Abstract

Superconductivity is a macroscopic quantum state characterized by dissipationless electrical transport and magnetic flux expulsion below a critical temperature. In this thesis, we study thin and narrow superconducting rings using a Stiffnessometer designed to probe the response of the superconducting condensate to a magnetic vector potential. In particular, we will determine the relevant length scales: London penetration depth λ, Pearl length Λ, and superconducting coherence length ξ.

In previous work in our group, ξ was estimated using a mean field approximate relation in which the critical flux depends mainly on the destruction of the order parameter magnitude. In this case, the outer radius of the ring is the decisive parameter. In this thesis, we show that this approximation does not capture the full physical picture, and the stability of the solution must be taken into account via fluctuations. In this approach, the inner radius plays the major role, but the critical flux depends on the complete ring geometry, including both the inner and outer radii, as well as on the Pearl length. Using the measured critical flux together with recent theoretical developments, we extracted ξ for two sets of MoSi superconducting ring geometries. For rings with constant outer radius, the analysis yielded $\xi = 15.2 \pm 0.4$ nm and for rings with constant inner radius $\xi = 14.1 \pm 0.2$ nm. The consistency between these values paves the way for accurate ξ measurements in other materials.

In addition, some samples showed sharp and periodic magnetic-moment jumps as the vector potential was increased. These jumps reduced the measured magnetic moment close to zero, indicating a strong suppression of the superconducting current during each transition. The jump periodicity depended on temperature and ring geometry, suggesting that the instability is related to changes in the superconducting phase and to transitions between metastable current-carrying states.

Overall, this work demonstrates the use of stiffnessometer measurements to extract superconducting length scales in thin rings and highlights the importance of geometric and screening effects in interpreting the critical response of superconducting annuli.

Abbreviations and Notations

Abbreviations

BCS	:	Bardeen–Cooper–Schrieffer theory
CGS	:	Centimeter–gram–second system of units
DC	:	Direct current
GFC	:	Gauge Field Cooling
GL	:	Ginzburg–Landau theory
MKS	:	Meter–kilogram–second system of units
MoSi	:	Molybdenum silicide
MPMS3	:	Magnetic Property Measurement System, third generation
PDE	:	Partial differential equation
RIE	:	Reactive ion etching
SQUID	:	Superconducting Quantum Interference Device
TMAH	:	Tetramethylammonium hydroxide
VSM	:	Vibrating Sample Magnetometry
ZGFC	:	Zero Gauge Field Cooling

Notation

ψ	:	Superconducting order parameter
ψ_0	:	Equilibrium superconducting order parameter
φ	:	Phase of the superconducting order parameter
$\delta\psi$	:	Fluctuation of the superconducting order parameter
$\delta\sigma_k$	:	Amplitude of the kth angular Fourier mode of the order-parameter fluctuation
k	:	Integer angular Fourier-mode index
ρ_s	:	Superconducting stiffness
ξ	:	Superconducting coherence length
λ	:	London penetration depth
Λ	:	Pearl length, $\Lambda = \lambda^2/d$
Φ_0	:	Superconducting flux quantum
$\mathbf{A}_{\text{tot}}$	:	Total magnetic vector potential
$\mathbf{A}_{\text{sc}}$	:	Vector potential generated by the superconducting screening currents
$\mathbf{A}_{\text{coil}}$	:	Vector potential generated by the excitation coil
J	:	Applied flux number, $J = \Phi/\Phi_0$
J_c	:	Critical applied flux number
j	:	Superconducting current density
x	:	Rescaled radial coordinate, $x = r/(J\xi)$
x_{in}	:	Rescaled inner radius, $x_{\text{in}} = r_{\text{in}}/(J\xi)$
x_{out}	:	Rescaled outer radius, $x_{\text{out}} = r_{\text{out}}/(J\xi)$
r_{in}	:	Inner radius of the superconducting ring
r_{out}	:	Outer radius of the superconducting ring
$P(r_{\text{in}}, r_{\text{out}}, \Lambda)$	:	Dimensionless geometry-dependent scaling factor
R_{pl}	:	Radius of the gradiometer pickup loop
p	:	Gauge-invariant momentum, $p = \nabla\varphi - \mathbf{A}$
p_c	:	Critical gauge-invariant momentum
ΔL	:	Change in fluxoid or winding number during a flux jump
$\tau_{\lvert\psi\rvert}$	:	Relaxation time of the order-parameter magnitude
τ_φ	:	Relaxation time of the superconducting phase

Chapter 1

Introduction

1.1 Superconductivity

Superconductivity is a distinct phase of matter characterized by two simultaneous phenomena that occur when a material is cooled below a specific critical temperature (T_c): the complete disappearance of electrical resistance ($\rho = 0$) and the Meissner effect, which is the perfect expulsion of all magnetic flux (perfect diamagnetism) from the interior of the material ($B = 0$) for small enough applied field. This unique state is fundamentally a quantum mechanical phenomenon, primarily explained by the microscopic Bardeen–Cooper–Schrieffer (BCS) theory [1]. The other leading theory which is a phenomenological one is of Ginzburg-Landau theory. Superconductors are classified into two main types based on their response to an applied external magnetic field ($\mathbf{H}$) which are called type I and type II. Each type behaves differently: type I shows perfect diamagnetism for magnetic fields lower than a critical value H_c and above it the superconductivity disappears. type II has two critical magnetic fields denoted as $H_{c,1}$ and $H_{c,2}$. Below $H_{c,1}$ we see perfect diamagnetism and above $H_{c,1}$ the magnetic field is quantized into magnetic flux lines called vortices which ”destroy” the superconductor and let the magnetic field penetrate creating a mixed state of superconductivity and normal state in a sample. At $H_{c,2}$ the superconductivity disappears [2].

1.1.1 Ginzburg–Landau equations

Ginzburg–Landau equations are using two length scales: the coherence length ξ and the London penetration depth λ_L, and introduce a complex order parameter ψ. The coherence length is the scale over which the order parameter changes. The London penetration depth is the length over which the magnetic field decays exponentially inside the superconductor. The order parameter deep inside the superconductor is often referred to as ψ_∞.

The Ginzburg–Landau theory is derived from the following free energy in MKS [2].

$$E = \int \left[f_{n0} + \alpha \left|\psi\right|^2 + \frac{\beta}{2} \left|\psi\right|^4 + \frac{1}{2m^*} \left|\left(-i\hbar\nabla - e^* A\right)\psi\right|^2 + \frac{B^2}{2\mu_0} \right] dx^n \tag{1.1}$$

where α and β are phenomenological parameters, α is a temperature dependent and β is temperature independent. $\hbar$ is the reduced Planck constant, A is the total vector potential, and B is the magnetic field. m^* and e^* are the effective Cooper-pair mass and charge. The GL equations are obtained by minimizing the free energy with respect to two variables: the vector potential and the order parameter. This leads to two GL equations:

$$\alpha\psi + \beta\left|\psi\right|^2\psi + \frac{1}{2m*}\left(\frac{\hbar}{i}\vec{\nabla} - e^*\vec{A}\right)^2\psi = 0 \tag{1.2}$$

$$\vec{j} = \frac{e^*\hbar}{2m^*i}\left(\psi^\dagger\vec{\nabla}\psi - \psi\vec{\nabla}\psi^\dagger\right) - \frac{e^{*2}}{m^*}\psi^\dagger\psi\vec{A}. \tag{1.3}$$

1.1.2 London equation

Historically the London equation was phenomenological discovered and one can show that it is a reduced case of the Ginzburg–Landau equations using

$$\psi(\vec{r}) = |\psi(\vec{r})|e^{i\phi(\vec{r})}. \tag{1.4}$$

It describes the supercurrent density as a function of the gauge field and the gradient of the order parameter [2].

$$\vec{j_s} = -\rho_s\left(\vec{A_{tot}} - \frac{\Phi_0}{2\pi}\vec{\nabla}\phi\right) \tag{1.5}$$

where ρ_s is the superconducting stiffness, $\vec{A_{tot}}$ is the magnetic vector potential, Φ_0 is the superconducting flux quantum, and, following the Ginzburg–Landau complex order parameter, ϕ is its phase (a scalar field).

Above the critical temperature the order parameter is zero as the material isn't superconducting. Below the critical temperature, in the GL framework, $|\psi|^2$ is proportional to the density of superconducting charge carriers. The relation between the order parameter and the stiffness ρ_s

$$\rho_s = \frac{|\psi|^2 e^{*2}}{m^*} = \frac{1}{\mu_0\lambda_L^2} \tag{1.6}$$

where e^* is the charge of the superconducting carriers, m^* is their mass, λ_L is London penetration length and μ_0 is the vacuum permeability.

1.2 Stability criterion for critical flux in a thin superconducting annulus

As mentioned above, in this work we examine experimentally a new, unpublished, theory of Roy Rabaglia, Amit Keren, and Ari Turner. In this section we outline the theory as was explained to me by Roy Rabaglia.

We model the superconducting annulus using the Ginzburg–Landau free-energy functional. In cgs units, the energy is written as

$$E = \int d^2r\left[\frac{\hbar^2}{2m^*}\left|\left(\nabla - \frac{ie^*}{\hbar c}\mathbf{A}\right)\psi\right|^2 - \alpha|\psi|^2 + \frac{\beta}{2}|\psi|^4 + \frac{1}{8\pi}|\nabla\times\mathbf{A}|^2\right], \tag{1.7}$$

The total vector potential is the sum of the externally applied vector potential and the vector potential generated by the screening currents in the superconductor,

$$\mathbf{A} = \frac{\Phi}{2\pi r}\hat{\boldsymbol{\theta}} + \mathbf{A}_{\mathrm{sc}}. \tag{1.8}$$

We define the number of applied flux quanta as

$$J = \frac{\Phi}{\Phi_0}, \tag{1.9}$$

where Φ_0 is the flux quantum.

We rescale the variables according to

$$\tilde{\mathbf{A}} = \frac{2\pi\xi}{\Phi_0}\mathbf{A}, \qquad x = \frac{r}{J\xi}, \qquad \tilde{\psi} = \sqrt{\frac{\beta}{\alpha}}\psi, \tag{1.10}$$

In these units, the external coil contribution becomes

$$\tilde{\mathbf{A}}_{\mathrm{coil}} = \frac{1}{x}\hat{\boldsymbol{\theta}}. \tag{1.11}$$

For a thin superconducting film, $d \ll \lambda$, where d is the film thickness, the Pearl length [3] is

$$\Lambda = \frac{\lambda^2}{d}. \tag{1.12}$$

In this limit, the magnetic-field energy associated with the self-field is small compared with the kinetic and condensation terms. Neglecting this contribution and omitting tildes for notational simplicity, the reduced free energy becomes

$$E = \int d^2x \left[\left| \left(\frac{1}{J}\nabla - i\mathbf{A} \right) \psi \right|^2 - |\psi|^2 + \frac{1}{2}|\psi|^4 \right]. \tag{1.13}$$

For $J \gg 1$, the spatial derivative of the equilibrium solution may be neglected in the zeroth-order minimization. The energy then reduces locally to

$$E = \int d^2x \left[-\left(1 - |A|^2\right)|\psi|^2 + \frac{1}{2}|\psi|^4 \right]. \tag{1.14}$$

Minimizing Eq. (1.14) with respect to $|\psi|$ gives the mean field solution

$$|\psi_0(x)|^2 = 1 - |A(x)|^2. \tag{1.15}$$

Choosing the equilibrium order parameter to be real and positive, we obtain

$$\psi_0(x) = \sqrt{1 - |A(x)|^2}. \tag{1.16}$$

This solution exists only where

$$|A(x)| < 1. \tag{1.17}$$

However, the condition $|A| < 1$ only ensures that the local superconducting solution exists. It does not by itself guarantee that the solution is stable. To determine stability, one must examine the second variation of the free energy.

1.2.1 Fluctuation analysis and the stability condition

We consider a small fluctuation around the mean field solution,

$$\psi(x,\theta) = \psi_0(x) + \delta\psi(x,\theta). \tag{1.18}$$

Because the annulus is azimuthally symmetric, the fluctuation can be decomposed into angular Fourier modes,

$$\delta\psi(x,\theta) = \sum_k \delta\sigma_k(x) e^{ik\theta}, \qquad k \in \mathbb{Z}. \tag{1.19}$$

Here, the functions $\delta\sigma_k(x)$ are the fluctuation amplitude and independent of θ and k is an integer. The zeroth-order term in the expansion of the free energy gives the energy of the unperturbed solution. The first-order terms vanish because ψ_0 satisfies the Euler–Lagrange equation. Therefore, the stability of the superconducting state is determined by the quadratic contribution in $\delta\psi$.

Keeping terms up to second order in the fluctuation gives

$$\delta E = \int d^2x \left[\frac{1}{J^2} \left| \frac{\partial \delta\psi}{\partial x} \right|^2 + \left| \left(\frac{1}{Jx}\frac{\partial}{\partial\theta} - i|\mathbf{A}| \right) \delta\psi \right|^2 + \frac{1}{2}\left(\psi_0^2 \delta\psi^2 + 2(2\psi_0^2 - 1)|\delta\psi|^2 + \psi_0^2 \delta\psi^{*2} \right) \right]. \tag{1.20}$$

Substituting expansion Equation 1.19 into Equation 1.20 gives

$$\begin{aligned} \delta E = \sum_{k,k'} \int d^2x \Bigg[& \frac{1}{J^2} \frac{\partial \delta\sigma_k}{\partial x} \frac{\partial \overline{\delta\sigma_{k'}}}{\partial x} e^{i(k-k')\theta} \\ & + \left(i\frac{k}{Jx} - i|\mathbf{A}| \right) \left(-i\frac{k'}{Jx} + i|\mathbf{A}| \right) \delta\sigma_k \overline{\delta\sigma_{k'}} e^{i(k-k')\theta} \\ & + \frac{1}{2}\left(\psi_0^2 e^{i(k+k')\theta} \delta\sigma_k \delta\sigma_{k'} + 2(2\psi_0^2 - 1) e^{i(k-k')\theta} \delta\sigma_k \overline{\delta\sigma_{k'}} + \psi_0^2 e^{-i(k+k')\theta} \overline{\delta\sigma_k}\, \overline{\delta\sigma_{k'}} \right) \Bigg]. \end{aligned} \tag{1.21}$$

Using the angular orthogonality relation

$$\int_0^{2\pi} e^{i(k-k')\theta}\, d\theta = 2\pi \delta_{k,k'}, \tag{1.22}$$

we obtain

$$\begin{aligned} \delta E = \sum_k \int d^2x \Bigg[& \frac{1}{J^2} \frac{\partial \delta\sigma_k}{\partial x} \frac{\partial \overline{\delta\sigma_k}}{\partial x} + \left(\left(\frac{k}{Jx} - |\mathbf{A}| \right)^2 + 2\psi_0^2 - 1 \right) \delta\sigma_k \overline{\delta\sigma_k} \\ & + \frac{1}{2}\psi_0^2 \left(\delta\sigma_k \delta\sigma_{-k} + \overline{\delta\sigma_k}\, \overline{\delta\sigma_{-k}} \right) \Bigg]. \end{aligned} \tag{1.23}$$

In the large-J limit, the radial-gradient term can be neglected compared with the angular contribution. Since the energy couples the k and $-k$ modes, it is useful to write it as a sum over positive values of k:

$$\delta E = \sum_{k>0} \int d^2x \Bigg[\left(\left(\frac{k}{Jx} - |\mathbf{A}| \right)^2 + 2\psi_0^2 - 1 \right) \delta\sigma_k \overline{\delta\sigma_k}$$
$$+ \left(\left(-\frac{k}{Jx} - |\mathbf{A}| \right)^2 + 2\psi_0^2 - 1 \right) \delta\sigma_{-k} \overline{\delta\sigma_{-k}}$$
$$+ \psi_0^2 \left(\delta\sigma_k \delta\sigma_{-k} + \overline{\delta\sigma_k}\,\overline{\delta\sigma_{-k}} \right) \Bigg]$$
$$+ \int d^2x \left[\left(|\mathbf{A}|^2 + 2\psi_0^2 - 1 \right) \delta\sigma_0 \overline{\delta\sigma_0} + \frac{1}{2}\psi_0^2 \left(\delta\sigma_0^2 + \overline{\delta\sigma_0}^2 \right) \right]. \tag{1.24}$$

The last two terms correspond to $k = 0$. Using the equilibrium relation

$$\psi_0^2 = 1 - |\mathbf{A}|^2, \tag{1.25}$$

the $k = 0$ contribution becomes

$$\int d^2x \left[\psi_0^2 \delta\sigma_0 \overline{\delta\sigma_0} + \frac{1}{2}\psi_0^2 \left(\delta\sigma_0^2 + \overline{\delta\sigma_0}^2 \right) \right] = \frac{1}{2} \int d^2x \, \psi_0^2 \left(\delta\sigma_0 + \overline{\delta\sigma_0} \right)^2. \tag{1.26}$$

This term is non-negative, and therefore the $k = 0$ mode cannot drive the instability.

We now consider the coupled modes k and $-k$, with $k > 0$. Minimizing the energy with respect to the coupled fluctuation amplitudes gives

$$\left[\left(\frac{k}{Jx} - |\mathbf{A}| \right)^2 + 2\psi_0^2 - 1 \right] \delta\sigma_k + \psi_0^2 \overline{\delta\sigma_{-k}} = 0, \tag{1.27}$$

$$\left[\left(-\frac{k}{Jx} - |\mathbf{A}| \right)^2 + 2\psi_0^2 - 1 \right] \delta\sigma_{-k} + \psi_0^2 \overline{\delta\sigma_k} = 0. \tag{1.28}$$

Equivalently,

$$\overline{\delta\sigma_{-k}} = -\frac{\left(\frac{k}{Jx} - |\mathbf{A}| \right)^2 + 2\psi_0^2 - 1}{\psi_0^2} \delta\sigma_k, \tag{1.29}$$

$$\delta\sigma_{-k} = -\frac{\psi_0^2}{\left(\frac{k}{Jx} + |\mathbf{A}| \right)^2 + 2\psi_0^2 - 1} \overline{\delta\sigma_k}. \tag{1.30}$$

Substituting these relations back into the energy, and using Equation 1.25, gives

$$\delta E = \sum_{k>0} \int d^2x \left[\left(\frac{k}{Jx} \right)^2 \frac{\left(\frac{k}{Jx} \right)^2 + 2 - 6|\mathbf{A}|^2}{\left(\frac{k}{Jx} + |\mathbf{A}| \right)^2 + 1 - 2|\mathbf{A}|^2} \right] \delta\sigma_k \overline{\delta\sigma_k}. \tag{1.31}$$

The first angular mode that can become unstable is the $k = 1$ mode. Keeping the leading term in $1/J$ for this mode gives

$$\delta E_{k=1} \simeq \frac{2}{J^2} \int d^2x \, \frac{1}{x^2} \frac{1 - 3|\mathbf{A}(x)|^2}{1 - |\mathbf{A}(x)|^2} \left| \delta\sigma_1(x) \right|^2. \tag{1.32}$$

Therefore, the fluctuation energy can become negative when

$$|\mathbf{A}(x)|^2 > \frac{1}{3}, \tag{1.33}$$

which gives the instability criterion for the current-carrying state. As long as the superconducting solution exists, the denominator in Eq. (1.32) is positive:

$$1 - |A(x)|^2 > 0. \tag{1.34}$$

The superconducting state is stable only if the quadratic fluctuation energy is positive everywhere in the annulus. Hence the stability condition is

$$1 - 3|A(x)|^2 > 0, \tag{1.35}$$

or equivalently

$$|A(x)| < \frac{1}{\sqrt{3}}. \tag{1.36}$$

The instability first occurs at the point where $|A(x)|$ is maximal. For the annular geometry considered here, the magnitude of the vector potential decreases monotonically away from the inner edge. Therefore, the maximum occurs at the inner radius,

$$x = x_{in}. \tag{1.37}$$

The critical condition is therefore

$$\boxed{|A(x_{in})| = \frac{1}{\sqrt{3}}.} \tag{1.38}$$

This equation defines the critical applied flux number J_c.

The same condition can also be understood physically from the current density. In the reduced variables, the supercurrent is proportional to

$$j(x) \propto A(x)|\psi_0(x)|^2. \tag{1.39}$$

Using Eq. (1.15), this becomes

$$j(x) \propto A(x)\left(1 - |A(x)|^2\right). \tag{1.40}$$

The maximum sustainable current occurs when

$$\frac{d}{d|A|}\left[|A|\left(1 - |A|^2\right)\right] = 0. \tag{1.41}$$

Evaluating the derivative gives

$$1 - 3|A|^2 = 0, \tag{1.42}$$

and therefore

$$|A| = \frac{1}{\sqrt{3}}. \tag{1.43}$$

Thus, the fluctuation analysis and the maximum-current argument give the same result. The superconducting state becomes unstable when the vector potential at the inner edge reaches the value for which the annulus can no longer support the required screening current.

1.2.2 Self-consistent vector potential and extraction of J_c

The critical condition in Eq. (1.38) is not yet an explicit expression for J_c, because the vector potential $A(x)$ must be found self-consistently. The total vector potential contains both the external contribution and the screening contribution from the superconductor:

$$A(x) = A_{\text{coil}}(x) + A_{\text{sc}}(x). \tag{1.44}$$

In the rescaled variables,

$$A_{\text{coil}}(x) = \frac{1}{x}. \tag{1.45}$$

To calculate A_{sc}, the annulus is divided into infinitesimal circular current rings of width $d\ell$. The current in each ring generates a vector potential. Each strip is treated as a narrow current loop located at radius ℓ. The local current in this loop is determined by the Ginzburg-Landau current density, and the vector potential produced by all such loops is then summed over the annulus.

We define the rescaled radius

$$\tilde{\ell} = \frac{\ell}{J\xi}, \qquad d\tilde{\ell} = \frac{d\ell}{J\xi}. \tag{1.46}$$

Here J is the applied flux number, while the superconducting current density is denoted by the lowercase symbol $\mathbf{j}$.

The Ginzburg–Landau current density is

$$\mathbf{j} = -\frac{e^{*2}}{m^*}\mathbf{A}|\psi|^2. \tag{1.47}$$

Using Equation 1.10, the current-density contribution of the strip at $\tilde{\ell}$ can be written as

$$\mathbf{j}_{\tilde{\ell}}(r,z) = -\frac{\Phi_0}{2\pi\mu_0}\frac{1}{\xi\Lambda}\tilde{A}(\tilde{\ell})\left(1 - |\tilde{A}(\tilde{\ell})|^2\right)\delta(z)\delta(r-\tilde{\ell})\,d\tilde{\ell}\,\hat{\theta}. \tag{1.48}$$

The delta functions express that the strip current is localized in the plane of the film and at the radius of the infinitesimal loop. The minus sign indicates that the superconducting current screens the applied vector potential.

The current carried by this infinitesimal loop is obtained by integrating the current density over the radial and vertical directions:

$$I_{\tilde{\ell}} = -\frac{\Phi_0}{2\pi\mu_0}\frac{J}{\Lambda}\tilde{A}(\tilde{\ell})\left(1 - |\tilde{A}(\tilde{\ell})|^2\right)\,d\tilde{\ell}. \tag{1.49}$$

Thus, each infinitesimal strip is replaced by a circular current loop whose current is fixed by the local value of the total vector potential.

The vector potential in the plane of the superconductor, produced by a circular loop of radius ℓ carrying current $di_{\tilde{\ell}}$, is given in [4, p. 142]

$$d\mathbf{A}_{\tilde{\ell}}(r, z=0) = \frac{\mu_0}{2\pi}I_{\tilde{\ell}}\left(1 + \frac{\ell}{r}\right)\left[\frac{\ell^2 + r^2}{(\ell + r)^2}K(k) - E(k)\right]\hat{\theta}, \tag{1.50}$$

where

$$k = \frac{2\sqrt{\ell r}}{\ell + r} = \frac{2\sqrt{\tilde{\ell}x}}{\tilde{\ell} + x}. \tag{1.51}$$

Here K and E are complete elliptic integrals of the first and second kind, respectively.

Finally, the superconducting contribution $A_{\rm sc}$ is obtained by integrating these loop contributions over the full annulus. From this point onward, the rescaled integration variable $\tilde{\ell}$ is denoted simply by ℓ. Combining this screening contribution with the external coil contribution, $\tilde{A}_{\rm coil}(x) = 1/x$, gives the self-consistent equation

$$|\tilde{A}(x)| = \frac{1}{x} - \frac{1}{2\pi}\frac{J\xi}{\Lambda}\int_{x_{in}}^{x_{out}} |\tilde{A}(\ell)|\left(1-|\tilde{A}(\ell)|^2\right)\left(1+\frac{\ell}{x}\right) \times\left[\frac{\ell^2+x^2}{(\ell+x)^2}K\left(\frac{2\sqrt{\ell x}}{\ell+x}\right) - E\left(\frac{2\sqrt{\ell x}}{\ell+x}\right)\right] d\ell. \tag{1.52}$$

The integration limits are

$$x_{in} = \frac{r_{in}}{J\xi}, \qquad x_{out} = \frac{r_{out}}{J\xi}. \tag{1.53}$$

Equation (1.52) makes clear how the annulus geometry affects the critical flux. The instability criterion is evaluated at the inner edge, $x = x_{in}$, because this is where the vector potential is largest. However, the value of $A(x_{in})$ depends on the screening currents throughout the entire annulus. Therefore, both the inner radius r_{in} and the outer radius r_{out} enter the calculation of J_c.

The procedure for extracting J_c is as follows. For a fixed annulus geometry, Eq. (1.52) is solved numerically for different values of J. For each value of J, the vector potential at the inner edge is evaluated at $|\tilde{A}(x_{in}; J)|$. The critical flux number is the value of J for which

$$|\tilde{A}(x_{in}; J_c)| = \frac{1}{\sqrt{3}}. \tag{1.54}$$

This is the interpretation of Fig. 1.1. Each curve shows the calculated value of $|\tilde{A}(x_{in})|$ as a function of the applied flux number J for a given ring geometry. The horizontal line marks the stability threshold

$$|\tilde{A}(x_{in})| = \frac{1}{\sqrt{3}}. \tag{1.55}$$

The intersection of each curve with this line gives the corresponding value of J_c.

The extracted critical values are summarized in Fig. 1.2. The leading trend is

$$J_c \propto \frac{r_{in}}{\xi}. \tag{1.56}$$

However, the proportionality factor is not strictly universal when the screening contribution of the annulus is included. More generally, one may write

$$J_c = P\left(r_{in}, r_{out}, \Lambda\right)\frac{r_{in}}{\xi}, \tag{1.57}$$

where P is a dimensionless geometry-dependent coefficient. The dependence on r_{out} arises because a wider annulus contains more superconducting material and therefore supports a different screening-current distribution. This modifies the total vector potential at the inner edge and shifts the value of J required to satisfy Eq. (1.54).

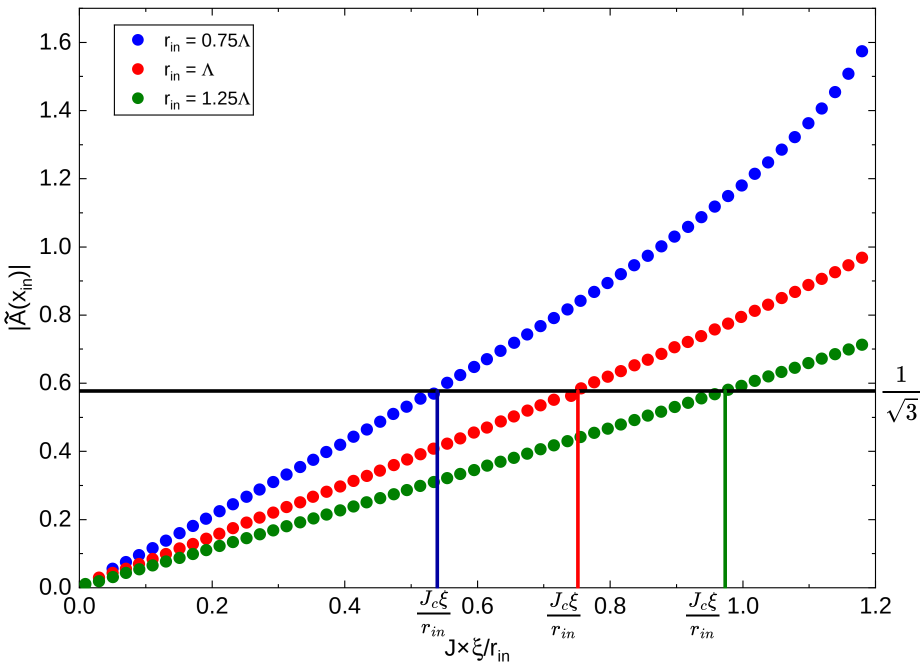

Figure 1.1: The value of the vector potential at the inner edge of the annulus, $|\tilde{A}(x_{in})|$, as a function of the applied flux number J, measured in units of Λ/ξ, for different ring geometries. In all cases shown here, $r_{out} = 4r_{in}$. The horizontal line marks the stability threshold $|\tilde{A}(x_{in})| = 1/\sqrt{3}$. For each ring, the critical flux number J_c is obtained from the intersection of $|\tilde{A}(x_{in})|$ with this threshold.

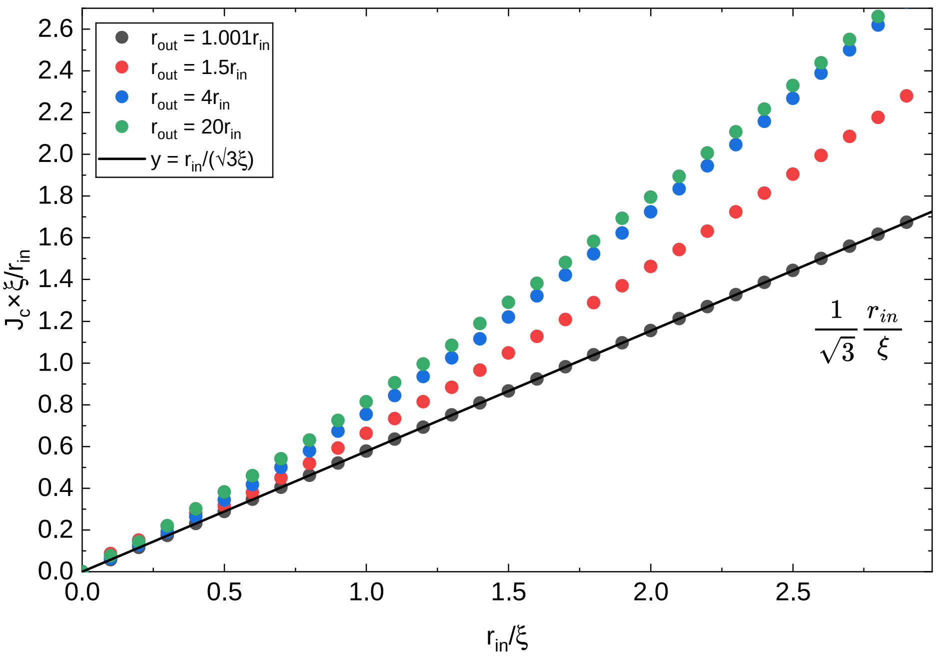

Figure 1.2: Normalized critical flux number J_c as a function of the normalized inner radius r_{in}/ξ for annuli with different ratios r_{out}/r_{in}. The black line corresponds to the thin and narrow annulus approximation, for which $J_c = r_{in}/(\sqrt{3}\xi)$, or equivalently $J_c = (r_{in}/\xi)/\sqrt{3}$. For wider annuli, the self-consistent vector potential generated by the superconducting screening currents modifies the value of $|\tilde{A}(x_{in})|$ and shifts the critical flux away from the narrow-ring limit.

1.2.3 Thin and very narrow annulus approximation

The fabricated devices considered in this work are thin superconducting rings, and in many cases the annular width is small compared with the inner radius. This motivates the thin, narrow, and very narrow annulus approximations. The thin-film condition is

$$d \ll \lambda, \tag{1.58}$$

The narrow-annulus condition is

$$r_{out} - r_{in} \ll r_{in}. \tag{1.59}$$

and the very-narrow-annulus condition is

$$\Lambda \gg \frac{1}{3\pi}(r_{out} - r_{in}) \ln\left(\frac{r_{in}}{r_{out} - r_{in}}\right). \tag{1.60}$$

In this limit, the magnetic-field energy associated with the self-field of the film is small compared to the coil magnetic-field energy.

In this case, the integration region in Eq. (1.52) is small, and the vector potential produced by the superconducting screening currents is weak compared with the applied coil contribution. Therefore,

$$|A_{\mathrm{sc}}| \ll |A_{\mathrm{coil}}|. \tag{1.61}$$

The total vector potential is then approximated by the external contribution alone:

$$|\tilde{A}(x)| \simeq \frac{1}{x}. \tag{1.62}$$

Substituting Eq. (1.62) into the critical condition, Eq. (1.38), gives

$$\frac{1}{x_{in}} = \frac{1}{\sqrt{3}}. \tag{1.63}$$

Using the definition

$$x_{in} = \frac{r_{in}}{J_c \xi}, \tag{1.64}$$

we obtain by solving for J_c

$$\boxed{J_c = \frac{1}{\sqrt{3}} \frac{r_{in}}{\xi}.} \tag{1.65}$$

Equivalently, if the critical flux number is measured experimentally, the coherence length can be extracted.

This result is especially useful for thin and very narrow fabricated rings because it gives a direct relation between the experimentally measured instability point and the coherence length. In this approximation, the critical flux is controlled primarily by the inner radius. The physical reason is that the vector potential is largest at the inner edge, so the depairing instability nucleates there first.

The outer radius r_{out} does not enter Eq. (1.65) explicitly because the self-consistent screening contribution has been neglected. However, this does not mean that r_{out} is always irrelevant. For wider rings, or for rings with stronger screening, the superconducting contribution A_{sc} becomes important. In that case, the full integral equation, Eq. (1.52), must be solved and the critical point is obtained from

$$|\tilde{A}(x_{in}; J_c)| = \frac{1}{\sqrt{3}}. \tag{1.66}$$

Thus, Eq. (1.65) should be viewed as the leading thin- and very-narrow-annulus limit, while deviations from this expression quantify the role of screening and finite ring width.

For the purposes of interpreting the fabricated thin and narrow rings (not very narrow), the main result is therefore Equation 1.57 with corrections that depend on the dimensionless ratios

$$\frac{r_{in}}{\Lambda}, \qquad \frac{r_{out}}{\Lambda}. \tag{1.67}$$

These corrections are more important when the ring is wide or when the Pearl length is comparable to the ring radius. In the limit of very-narrow ring $P \to 1/\sqrt{3}$. As we show below, we nearly obey this limit in our narrowest rings.

1.3 Mean field critical flux in a thin superconducting annulus

In this section we will describe the mean field approach to estimate the coherence length ξ; an approach that we find insufficient. This approach starts from the second GL equation

$$\xi^2 \left(\psi_{rr} + \frac{\psi_r}{r}\right) = \left(\xi^2 \left(A_{sc} + \frac{J}{r}\right)^2 - 1\right)\psi + \psi^3. \tag{1.68}$$

Here, the magnetic vector potential produced by the ring itself is assumed to be negligible compared with that generated by the excitation coil $A_{sc} \to 0$, $A_{ec} \propto \frac{J_c}{r}$ and ψ^3 is negligible, since we are looking for J that destroys ψ, leaving

$$\psi_{rr} + \frac{\psi_r}{r} = \left(\left(\frac{J}{r}\right)^2 - \frac{1}{\xi^2}\right)\psi. \tag{1.69}$$

For high flux J, ψ is zero near r_{in} and monotonically increases over distance ξ to a constant near r_{out}. Consequently, ψ_r decreases to zero towards r_{out} and $\psi_{rr}(r_{out}) \leq 0$. Therefore, the critical flux can be related to the coherence length according to [5, 6]

$$J_c = \frac{\Phi_c}{\Phi_0} \approx \frac{r_{out}}{\xi}. \tag{1.70}$$

1.4 Multiple Flux Jumps

Multiple flux jumps are commonly discussed in mesoscopic superconducting rings in the presence of an applied magnetic field, where the system can occupy several metastable fluxoid states. In such systems, the superconducting order parameter does not necessarily evolve continuously between neighboring states. Instead, a state with a given vorticity can remain metastable until the gauge-invariant momentum,

$$p = \nabla\phi - A, \tag{1.71}$$

reaches a critical value p_c. Physically, this condition corresponds to the point at which the kinetic energy of the Cooper pairs becomes comparable to their binding energy, so that the metastable superconducting state becomes unstable. Once this instability is reached, the system can relax not only to the nearest fluxoid state, but directly toward a lower-energy state, producing an avalanche-like transition. This can result in change of more than one in the fluxoid number and we denote the flux jump number as ΔL thus $\Delta L > 1$, rather than a sequence of single-fluxoid transitions [7, 8, 9].

The occurrence of multiple jumps is therefore not determined only by the existence of several metastable states, but also by the dynamics of the transition between them. In the time-dependent Ginzburg–Landau description, multiquanta jumps become possible when the relaxation time of the magnitude of the order parameter is much longer than the relaxation time of its phase [10], i.e.

$$\frac{\tau_{|\psi|}}{\tau_{\phi}} \gg 1. \tag{1.72}$$

Under this condition, the phase can change rapidly while the amplitude of the order parameter has not yet fully recovered, allowing the system to pass through several intermediate metastable states before stabilizing [11, 12, 13]. Although the experiment discussed here is performed without an externally applied magnetic field, a similar phenomenology may still be relevant. In the absence of a magnetic field, the instability is driven mainly by the phase gradient or supercurrent rather than by magnetic flux entry. The observed discrete jumps can therefore be interpreted as transitions between metastable superconducting configurations that occur once a current- or phase-driven instability threshold is reached. In this sense, the behavior is analogous to multiple flux jumps in superconducting rings, even though the control parameter in the present experiment is not an applied magnetic field.

Chapter 2

Stiffnessometer

The Stiffnessometer is an experimental apparatus specifically designed to measure the superconducting stiffness, ρ_s, and the superconducting coherence length, ξ. The configuration consists of a superconducting annulus positioned concentrically around a long, ideally infinite, excitation coil.

By driving a direct current (DC) through the excitation coil, a magnetic flux threads the center of the annulus. Consequently, the annulus experiences a magnetic vector potential, $\vec{A} = C(R_{pl})I\hat{\varphi}$ as $C(R_{pl})$ is determined experimentally, without direct exposure to a magnetic field H, as the field remains confined within the long excitation coil. This geometry induces supercurrents in the annulus due to the London equation [5, 14, 15].

There are two primary measurement protocols utilized with this setup:

1. Zero Gauge Field Cooling (ZGFC)

The ZGFC protocol sequence consists of:

1. Cooling the system to the desired base temperature.
2. Driving the target current through the excitation coil.
3. Measuring the resulting magnetic moment.

This protocol establishes the gauge of the magnetic vector potential such that $\vec{\nabla}\phi = 0$ within the London equation 1.5.

2. Gauge Field Cooling (GFC)

The GFC protocol proceeds as follows:

1. Driving the target current through the excitation coil.
2. Cooling the system to the desired base temperature.
3. Extinguishing (nulling) the current in the excitation coil.
4. Measuring the magnetic moment.

This protocol dictates that the total magnetic vector potential satisfies $\vec{A}_{tot} - \frac{\Phi_0}{2\pi}\vec{\nabla}\phi = 0$ at the beginning of the measurement within the London equation.

The applied magnetic vector potential induces supercurrents within the annulus, which in turn generate a measurable magnetic moment. We quantify this moment using a superconducting quantum interference device (SQUID) magnetometer. The inherent linearity of the London equation permits a clear distinction between the linear response regime and the constant response regime. The transition between these two states occurs precisely at the critical current of the excitation coil, $J = J_c$.

2.1 Obtaining Λ

To determine Λ, one must work in the $J \to 0$ limit where the theories presented above do not apply. We therefore begin with the two-dimensional representation of Equation 1.5. By substituting Ampere's law and the definition of the magnetic vector potential ($\vec{B} = \vec{\nabla} \times \vec{A}$), we obtain:

$$\vec{\nabla} \times \left(\vec{\nabla} \times \vec{A}_{SC}\right) = -\mu_0 \rho_s \vec{A}_{tot} \tag{2.1}$$

$$\nabla \left(\overbrace{\vec{\nabla} \cdot \vec{A}_{SC}}^{0}\right) - \nabla^2 \vec{A}_{SC} = -\mu_0 \rho_s \vec{A}_{tot} \tag{2.2}$$

$$\nabla^2 \vec{A}_{SC} = \mu_0 \rho_s \left(\vec{A}_{SC} + \vec{A}_{EC}\right) \tag{2.3}$$

$$\nabla^2 \vec{A}_{SC} = \mu_0 \rho_s \left(\vec{A}_{SC} + \frac{\Phi_{EC}\left(R_{pl}\right)}{2\pi r}\hat{\varphi}\right) \tag{2.4}$$

$$\frac{\partial^2 A}{\partial z^2} + \frac{\partial^2 A}{\partial r^2} + \frac{1}{r}\frac{\partial A}{\partial r} - \frac{A}{r^2} = \frac{1}{\Lambda^2}\left(\vec{A} + \frac{1}{r}\hat{\varphi}\right)\delta(z) \tag{2.5}$$

In line 2.2, we apply standard curl identities; in line 2.3, we adopt the London gauge; and in line 2.4, we substitute the expression for the magnetic vector potential of an infinite coil. Finally, in line 2.5, we utilize the system's cylindrical symmetry and normalize the variables such that $\frac{r}{R_{pl}} \to r$, $\frac{A_{SC}}{A_{EC}(R_{pl})} \to A$, and $\frac{\lambda}{R_{pl}} \to \lambda$ as R_{pl} is the radius of the pickup loop.

This represents the strong formulation of the partial differential equation (PDE) we wish to solve. We then convert this PDE into its weak formulation (via multiplication by a test function and integration by parts) and employ the FreeFEM++ solver. This allows us to compute the magnetic vector potential applied to the pickup loop, $A\left(R_{pl}\right)$, as a function of Λ. The normalized A is expressed as:

$$A\left(R_{pl}\right) = \frac{A_{SC}\left(R_{pl}\right)}{A_{EC}\left(R_{pl}\right)} = \frac{\frac{\mu_0 m}{4\pi R_{pl}}}{A_{EC}\left(R_{pl}\right)} = C \cdot \frac{m}{I} \tag{2.6}$$

where C is a constant that can be either calculated analytically or obtained directly from measurements. Consequently, the linear $\frac{m}{I}$ response allows for the direct retrieval of $A\left(R_{pl}\right)$.

Chapter 3

Sample Fabrication

The molybdenum silicide (MoSi) samples used in this work were fabricated from a MoSi target and 50 nm thick film deposited by sputtering. After deposition, the desired device geometry was defined by standard photolithography, followed by reactive ion etching (RIE) to remove the exposed MoSi and leave the final patterned structure. The fabrication process consisted of these main stages: sputtering, photoresist coating, ultraviolet exposure using the mask aligner, and development of the exposed resist. After these steps, the patterned resist served as an etching mask during the RIE process. MoSi was chosen for this study because of its critical temperature of approximately 7 K [16, 17, 18] and its room-temperature deposition process, which enables convenient and reproducible sample fabrication. In addition, MoSi has a relatively large penetration depth, with $\lambda \sim 4\ \mu$m [5, 19], making it well suited for studying the very narrow-ring limit described by Equation 1.60.

3.1 MoSi Thin-Film Sputtering

A MoSi thin film was deposited on the silicon ring substrate. The deposition was performed using an ATC2200 sputtering system, with a MoSi target used as the source material.

Sputtering is a physical vapor deposition technique in which energetic ions from a plasma are accelerated toward a target material. The ion bombardment removes atoms from the target surface, and these atoms then travel through the chamber and condense on the substrate, forming a thin film. In this work, the MoSi film was deposited in DC sputtering mode. In this configuration, a DC voltage is applied between the MoSi target and the substrate/chamber, producing a plasma and accelerating ions toward the target. The ejected MoSi species were then deposited onto the silicon sample surface.

The deposition was carried out at room temperature, without intentional substrate heating. This allowed the superconducting MoSi layer to be deposited while avoiding additional thermal processing of the silicon ring samples. After deposition, the samples consisted of a nominally 50 nm thick MoSi film on the silicon substrate.

3.2 Substrate Preparation and Photoresist Coating

The process was carried out as follows. First, a supporting wafer was coated with photoresist by dispensing a small amount of photoresist onto its surface, followed by spinning. The 5 mm diameter ring sample was then placed on top of the coated wafer and soft-baked. This bake helped attach the sample to the wafer and hold it in place during the following lithography steps. After the sample was fixed, photoresist was dispensed directly onto the sample surface, followed by spin coating and another soft bake.

3.3 Photolithographic Exposure

After the photoresist coating step, the sample was patterned by photolithographic exposure using a mask aligner. The photomask used in this work was specifically designed to define ring-shaped structures with a range of geometrical parameters, including multiple inner and outer diameters and ring widths. This design allowed the fabrication of several ring geometries on the same wafer, enabling systematic comparison between samples with different dimensions.

During the exposure step, the coated sample was aligned with the photomask and illuminated with ultraviolet light, transferring the ring patterns into the photoresist. The exact operational details of the aligner are omitted here, since only the general fabrication flow is relevant for the present thesis. The purpose of this stage was to accurately reproduce the designed ring array in the resist layer, which subsequently served as the etching mask for pattern transfer into the MoSi film.

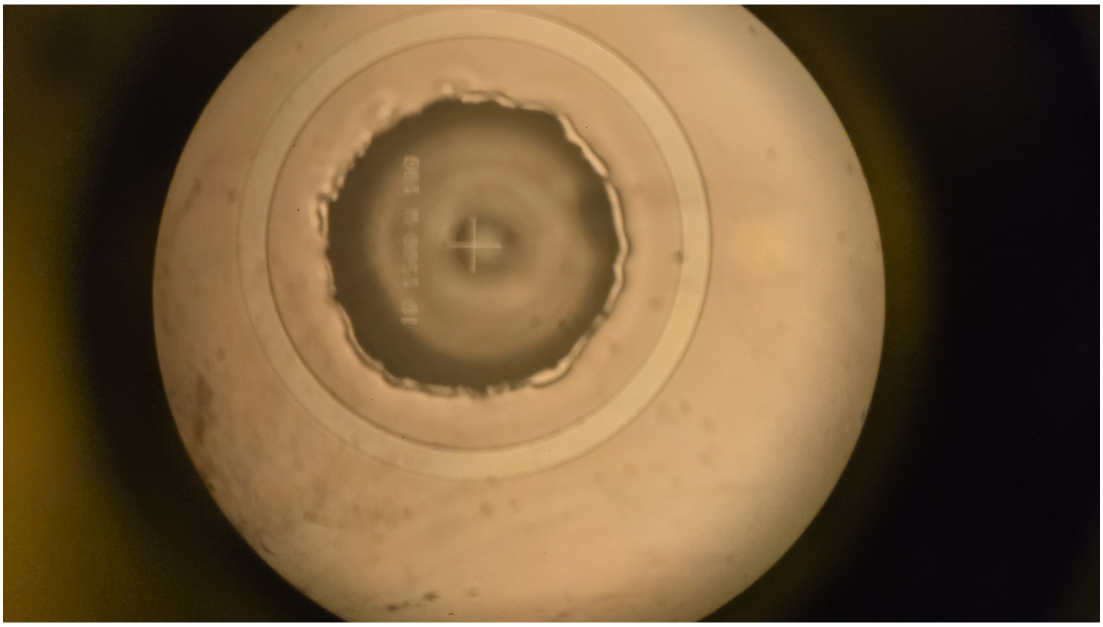

Figure 3.1: Alignment of the ring pattern over the sample prior to exposure.

3.4 Resist Development

Immediately after exposure, the sample underwent a post-exposure bake at 90 °C for 10 minutes. This step was found to be suitable for the MoSi samples used in this work.

The sample was then immersed in tetramethylammonium hydroxide (TMAH) developer for 1 minute while gently agitating the solution in order to promote uniform development. After development, the sample was rinsed in deionized water using a two-stage rinse procedure: it was first dipped in the "dirty" deionized water cascade, and then transferred to the "clean" side, where it was rinsed by approximately 30 short dips.

To dry the sample, the holder was first placed on absorbent paper, and the sample was then spin-dried at 4000 rpm. The resulting pattern was inspected, and the lithography process was repeated when necessary in order to improve pattern quality or alignment.

3.5 Reactive Ion Etching

Once the resist pattern was successfully defined, the sample was transferred to the reactive ion etching system. During this step, the exposed MoSi regions were etched away, while the photoresist protected the areas corresponding to the desired device geometry. In this way, the lithographically defined pattern was transferred into the superconducting MoSi film, yielding the final sample structure used for measurements. Figure 3.2 shows a microscope image of the ring sample after fabrication.

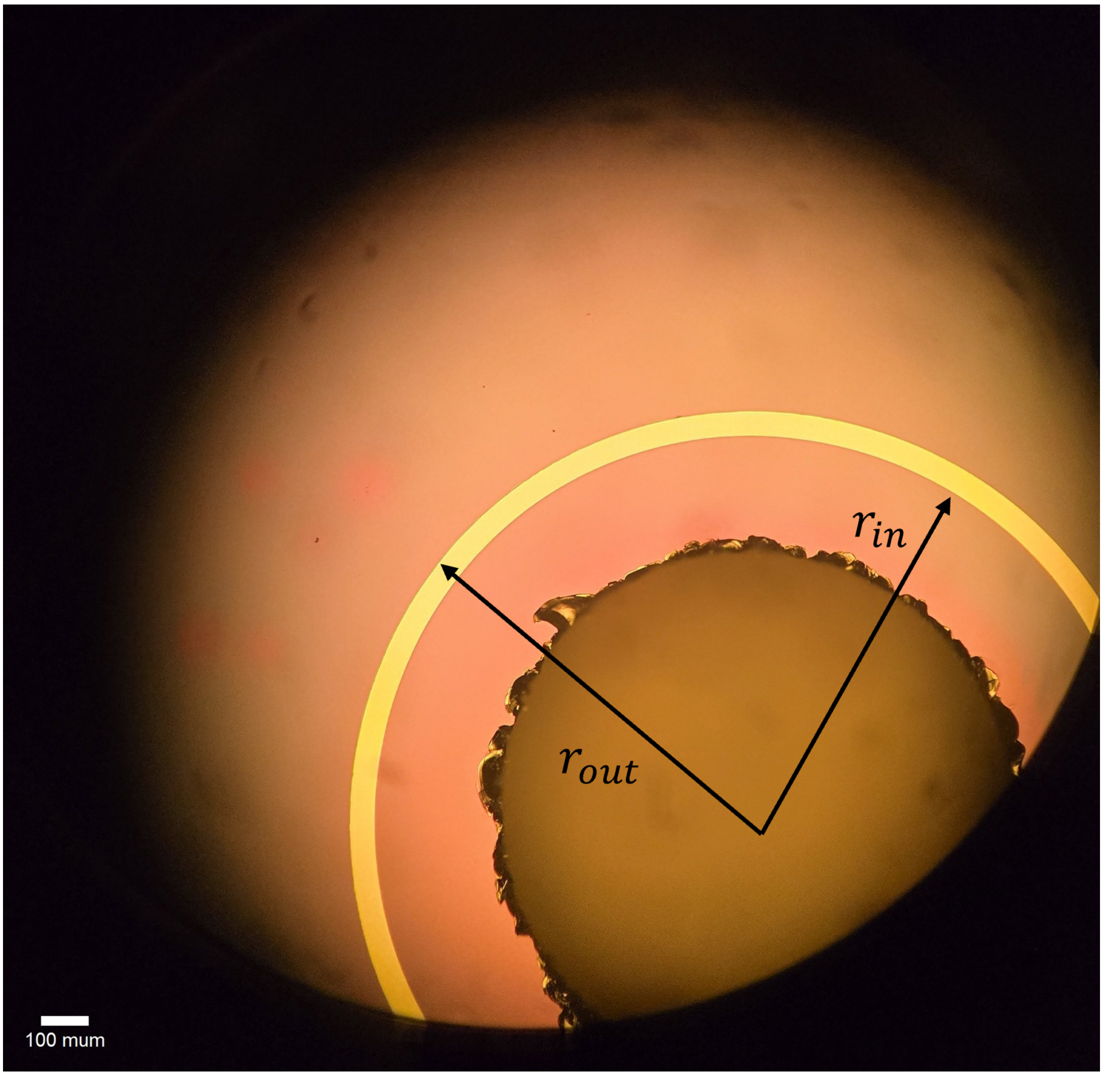

Figure 3.2: Ring after processing with $r_{in} = 750$ μm and $r_{out} = 800$ μm.

Chapter 4

System setup

4.1 Experimental Setup: The Stiffnessometer

The central experimental challenge in this work is the precise measurement of the superfluid density, ρ_s, which is proportional to the inverse square of the London penetration depth ($1/\Lambda$). To achieve this, we employ a "Stiffnessometer" configuration within a commercial SQUID magnetometer. This setup allows for the direct probing of the superconducting phase stiffness by measuring the magnetic response of a superconducting ring to a well-defined magnetic vector potential $\mathbf{A}$.

4.2 The MPMS3 SQUID System

The experiments are conducted using a **Quantum Design MPMS3 SQUID magnetometer**. This system provides a cryogen-free environment with millikelvin temperature stability and high-precision magnetic field control. The MPMS3 is equipped with an external superconducting coil capable of nulling the Earth's magnetic field and other ambient remanent fields to a level below 0.05 Oe, or applying a controlled external field for flux-entry studies [20].

Figure 4.1: Schematic depiction of the MPMS3 setup in the stiffnessometer configuration. The superconducting MoSi ring and the internal excitation coil (”inner coil”) are positioned relative to a second-order gradiometer and its radius is denoted as R_{pl}. The gradiometer is inductively coupled to a SQUID sensor.

The setup utilizes a distinct method for generating a **Rotor-free** magnetic vector potential **A** using a long excitation coil threading the annulus. This field-free vector potential ($\nabla \times \mathbf{A} = 0$) at the sample position, allows probing the phase stiffness without introducing vortices.

4.2.1 Measurement Modes: DC and VSM

The magnetic flux produced by the MoSi screening currents is recorded by a second-order gradiometer. We scan the sample along the z-axis (normal to the plane of the annulus) using two primary modes:

- **DC Mode:** The sample is moved through the gradiometer coils in a discrete ”step-and-measure” process. The SQUID records the flux $\Phi(z)$, which is subsequently fitted to a theoretical dipole-like response profile to extract the magnetic moment m.

- **VSM Mode (Vibrating Sample Magnetometry):** The sample is mechanically oscillated at a fixed frequency (typically 10–14 Hz) with a defined amplitude. The resulting oscillating voltage is detected via a lock-in amplifier. VSM mode generally offers superior sensitivity and faster data acquisition compared to DC mode.

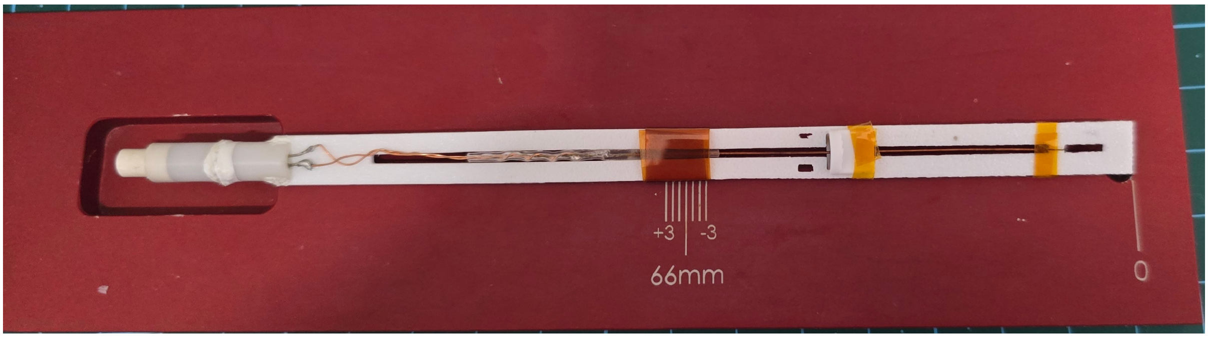

Figure 4.2: Stiffnessometer sample holder. The assembly includes the superconducting excitation coil made from NbTi with $T_c = 10$ K. The MoSi ring, secured by a specialized support piece to ensure concentricity.

4.2.2 The SQUID Detector Physics

The Superconducting Quantum Interference Device (SQUID) is the primary transducer in this experiment. It operates on the principle of flux quantization and Josephson tunneling. Our DC SQUID consists of a superconducting loop interrupted by two Josephson junctions. The critical current I through the SQUID is a periodic function of the threading flux Φ:

$$I(\Phi) = 2I_c \left|\cos\left(\frac{\pi\Phi}{\Phi_0}\right)\right| \tag{4.1}$$

where $\Phi_0 = h/2e \approx 2.067 \times 10^{-15}$ Wb is the magnetic flux quantum. By operating in a flux-locked loop, the SQUID converts the minute flux changes from the MoSi ring into a measurable voltage. The magnetic signal from our narrow MoSi samples was on the order of 10^{-7} emu, requiring the high sensitivity of a SQUID for reliable measurement.

Chapter 5

Experimental results

5.1 Stiffnessometer

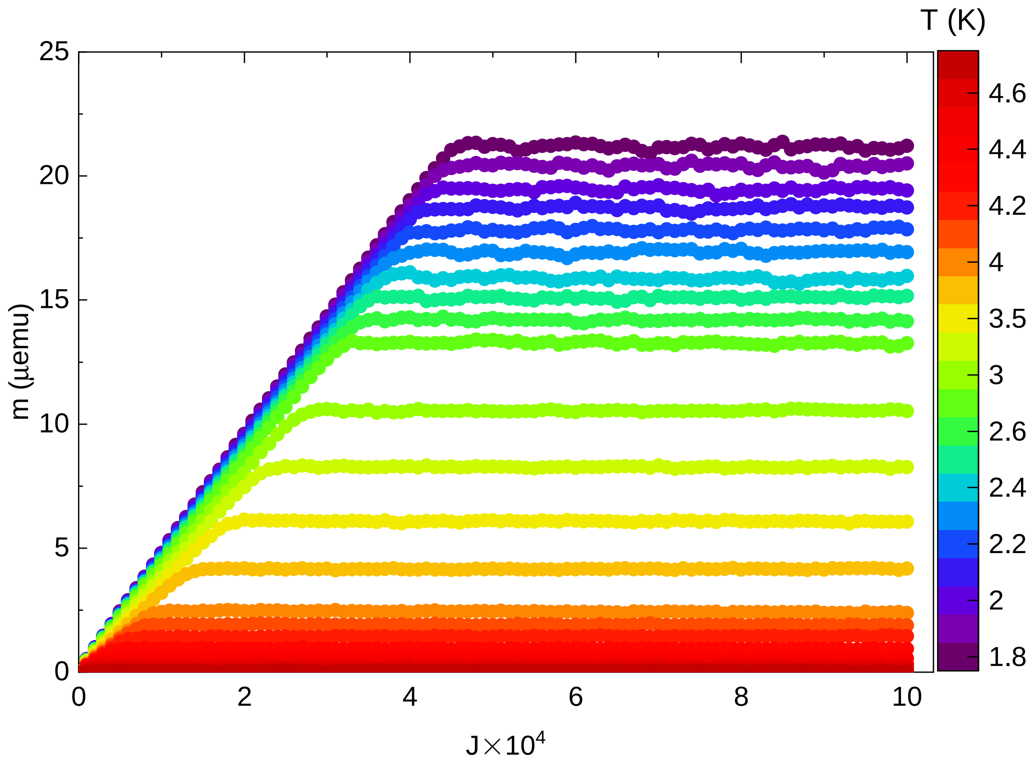

Figure 5.1: Reduced magnetic moment as a function of the excitation-coil flux number. At low flux, the response is approximately linear, while above the critical flux J_c the signal approaches a plateau. The color bar indicates the measurement temperature. The ring has an inner radius of 700 μm and an outer radius of 800 μm.

Figure 5.1 shows the reduced magnetic moment as a function of the flux applied to the excitation coil. To obtain the reduced moment, the magnetic contribution of the excitation coil was first measured above the critical temperature of the superconducting sample. The critical temperature varied between 4.7 and 7.1 K, depending on the sample. A linear fit to the measured response was used to determine the magnetic background generated per unit current applied to the excitation coil. This background contribution was then subtracted from the total measured magnetic moment.

From the measurement at 1.8 K, the magnetic moment initially shows an approximately linear dependence on the excitation-coil current up to about 20 mA, corresponding to $J = 4.3 \cdot 10^4$. Above this current, the magnetic moment saturates and remains nearly constant at approximately 22 μemu. This saturation indicates that the ring has reached its critical magnetic moment. Beyond this point, additional flux introduced by the excitation coil is accommodated through the entry of vortices into the superconducting ring, allowing the ring to remain close to equilibrium rather than further increasing its magnetic moment. Therefore, the flux number at which the magnetic moment reaches this saturation value is identified as the critical flux.

5.1.1 Obtaining Λ

After solving Equation 2.5 in FreeFEM++ [21] for the specific ring geometry, we calculate the magnetic-response slope as a function of the Pearl length. The experimentally measured slope is then converted to vector-potential units and compared with the numerical result. Finally, a one-dimensional interpolation is performed to extract the Pearl length of the ring, as shown in Figure 5.2.

Figure 5.3 shows Λ as a function of temperature. As expected, Λ increases with increasing temperature, and around 3 K it becomes larger than the ring width of 100 μm.

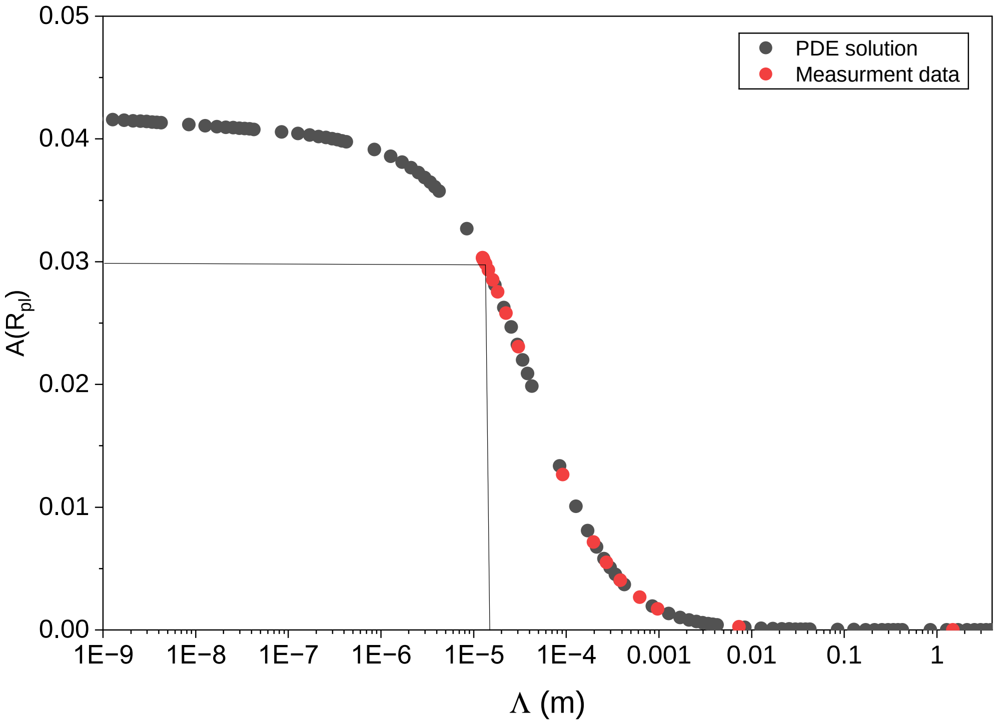

Figure 5.2: $A(R_{pl})$ as a function of Λ, R_{pl} is the gradiometer loop radius. The gray points represent the PDE solution obtained from Equation 2.5 for a 75 μm-wide ring with an inner radius of 750 μm, and various values of Λ. The red points represent the experimental measurements for the same ring dimensions. Each experimental point corresponds to a different temperature in the range 1.8–6.8 K, with the smallest Λ corresponding to the lowest temperature. The solid lines illustrate an example of the one-dimensional interpolation used to match the measured A to the PDE solution and determine the corresponding Λ.

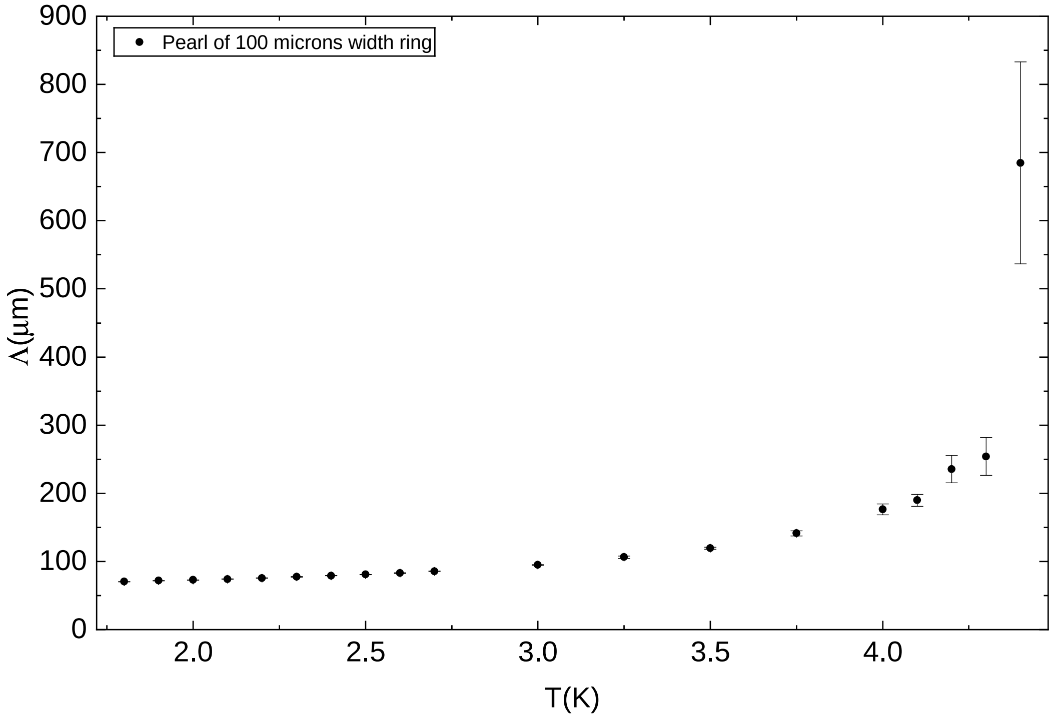

Figure 5.3: Pearl length as a function of temperature for a ring with inner radius 700 μm and outer radius 800 μm. The Pearl length shows a rapid increase near the critical temperature, around 4.7 K.

5.1.2 Obtaining ξ

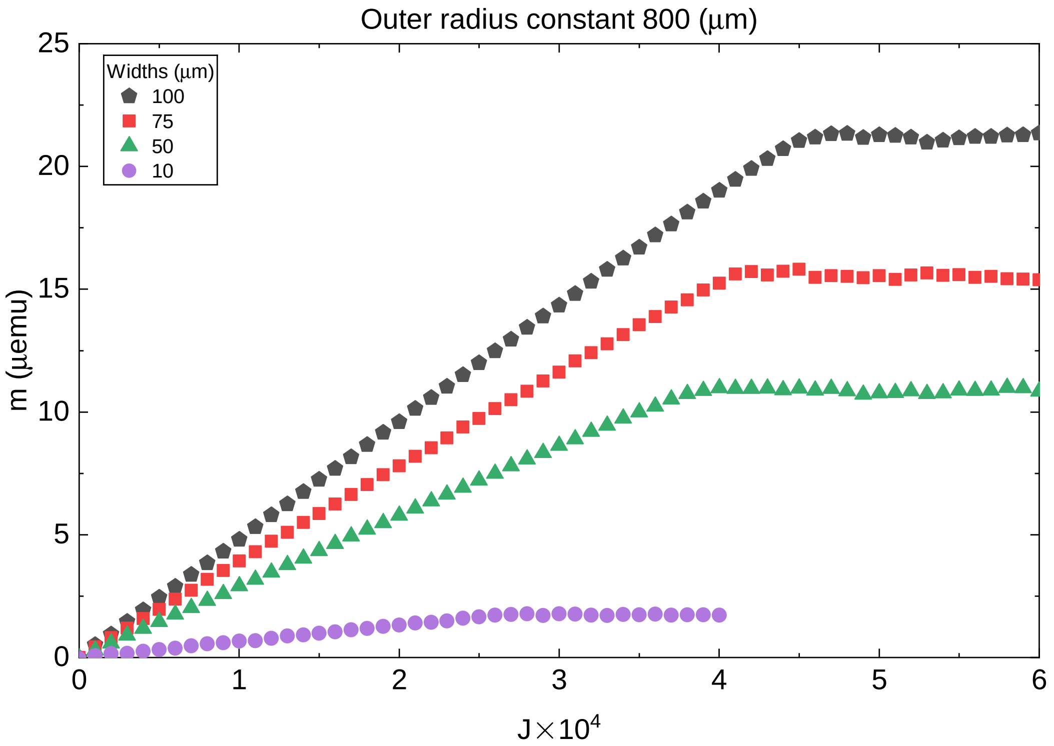

Figure 5.4: Magnetic response as a function of excitation coil flux number for four samples measured at 1.8 K. All samples share a constant outer radius of 800 μm but have varying inner radii, corresponding to track widths of 100, 75, 50, and 10 μm.

In Figure 5.4, the magnetic response to the excitation coil flux number is shown for rings with different widths. Both the initial response slope and the critical magnetic moment decrease as the ring width becomes smaller. For each ring, measurements similar to those shown in Figure 5.1 were performed, and the corresponding Pearl length, Λ, was extracted using the procedure described above.

Using Equation 1.57, we aim to extract the coherence length, ξ. To do so, we first computed the normalized vector potential for each ring geometry and determined the corresponding dimensionless geometry-dependent scaling coefficient. After obtaining this coefficient for each ring, ξ was extracted from the slope of the linear fit of the critical flux, J_c, as a function of $P \cdot r_{in}$.

From Figure 5.5, the inverse slope of the linear fit gives a coherence length of $\xi = 15.2 \pm 0.4$ nm. However, not all data points lie exactly on the regression line. In particular, the ring with a width of 10 μm shows the largest deviation. This suggests that the numerical prefactor used in the calculation does not fully capture the geometry-dependent correction required for this narrow ring to follow the same linear trend.

It should also be noted that the 75 μm and 50 μm rings were fabricated from the same original ring. After the 75 μm ring was measured, it was further patterned into a 50 μm ring. This ring showed the best agreement with the linear fit.

The same analysis was then repeated for a second set of rings, in which the inner radius

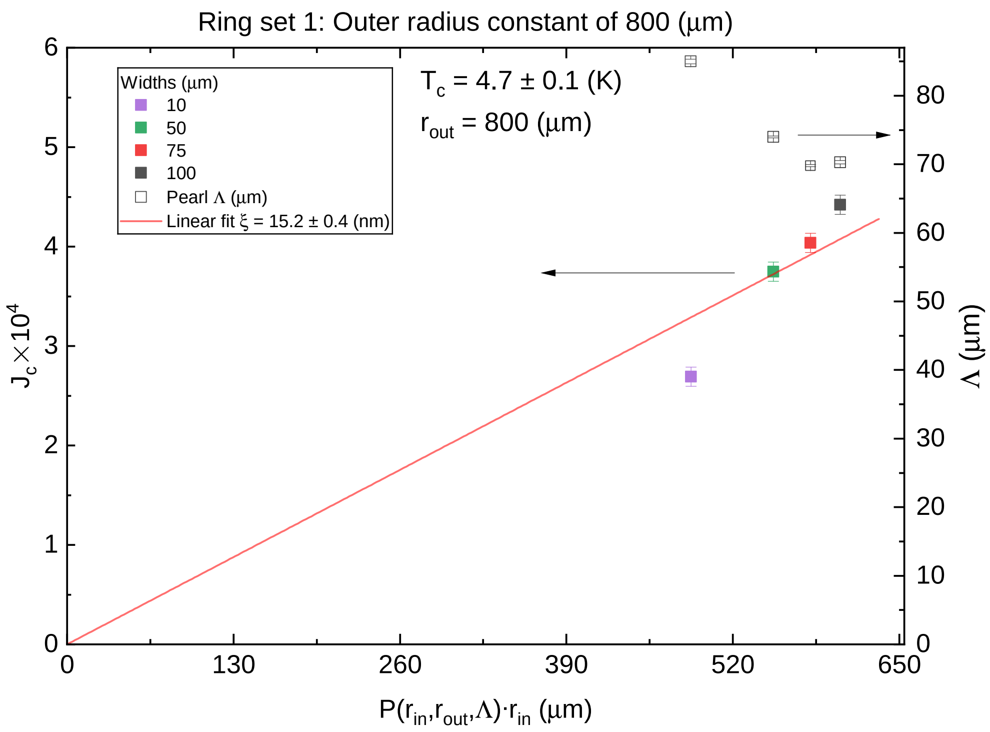

Figure 5.5: Critical flux, J_c, as a function of the inner radius multiplied by the geometric factor $P(r_{in}, r_{out}, \Lambda) \cdot r_{in}$ as defined in Equation 1.57. Solid data points correspond to the left axis and show measurements for multiple rings with a constant outer radius $r_{out} = 800$ μm and varying widths. The inverse of the slope from the linear fit through the origin yields a coherence length of $\xi = 15.2 \pm 0.4$ nm. Hollow data points correspond to the right axis and represent the calculated Pearl length, Λ, for each ring.

was held constant at 750 μm while the outer radius was varied. Figure 5.6 shows the magnetic response measured for each ring at 1.8 K. Similar to the set of rings with constant outer radius, the critical flux number at which the critical magnetic moment is reached decreases as the ring width is reduced.

However, the critical moments measured for the rings with constant inner radius are significantly larger than those measured for the rings with constant outer radius. For example, the ring with inner radius 750 μm and outer radius 850 μm has a critical moment of approximately $m_c \approx 115$ μemu, as shown in Figure 5.6. In comparison, the ring with inner radius 700 μm and outer radius 800 μm has a critical moment of approximately $m_c \approx 23$ μemu. This difference is mainly attributed to the fact that the two sets of samples were sputtered in different batches and therefore had different material properties. In particular, the critical temperature of the rings with constant outer radius was approximately 4.7 K, whereas the rings with constant inner radius had a critical temperature of approximately 6.8 K.

After computing the geometry factor for each data point in Figure 5.6, the normalized data were plotted in Figure 5.7. As in the previous set of rings, the narrower rings, with widths of 30 μm and 10 μm, show larger deviations from the linear fit, while the wider rings agree better with the expected linear behavior.

Table 5.1 summarizes the results extracted for each data point shown in Figure 5.7 and

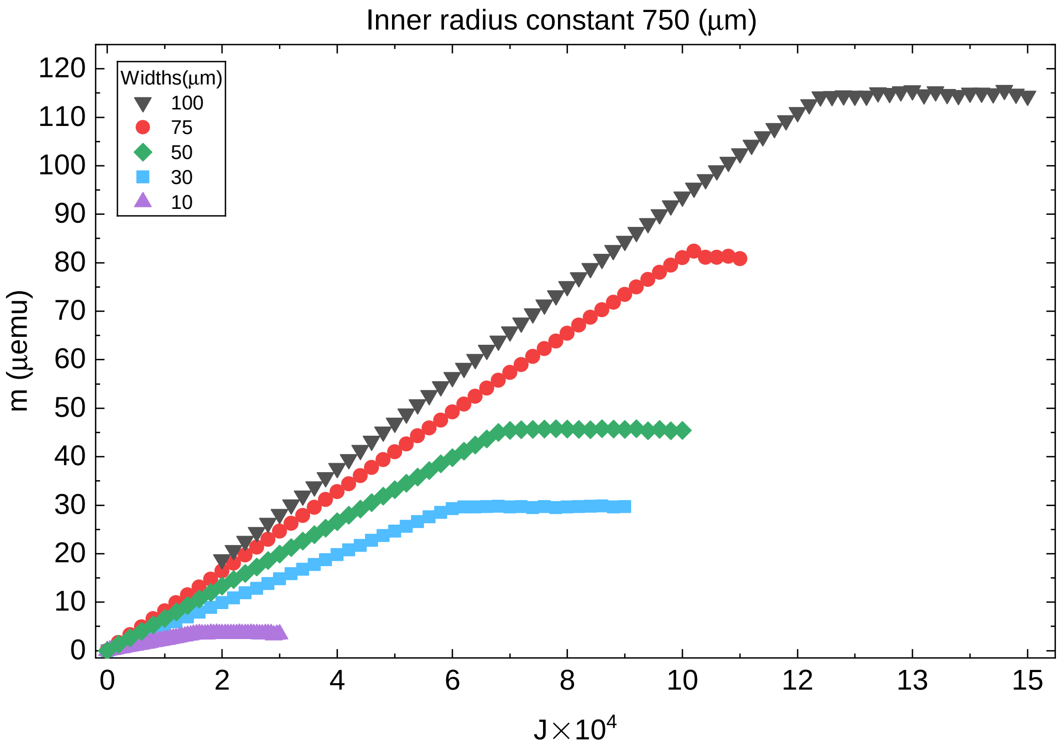

Figure 5.6: Magnetic response as a function of excitation coil flux number for five samples measured at 1.8 K. All samples share a constant inner radius of 750 μm but have varying outer radii, corresponding to track widths of 100, 75, 50, 30, and 10 μm.

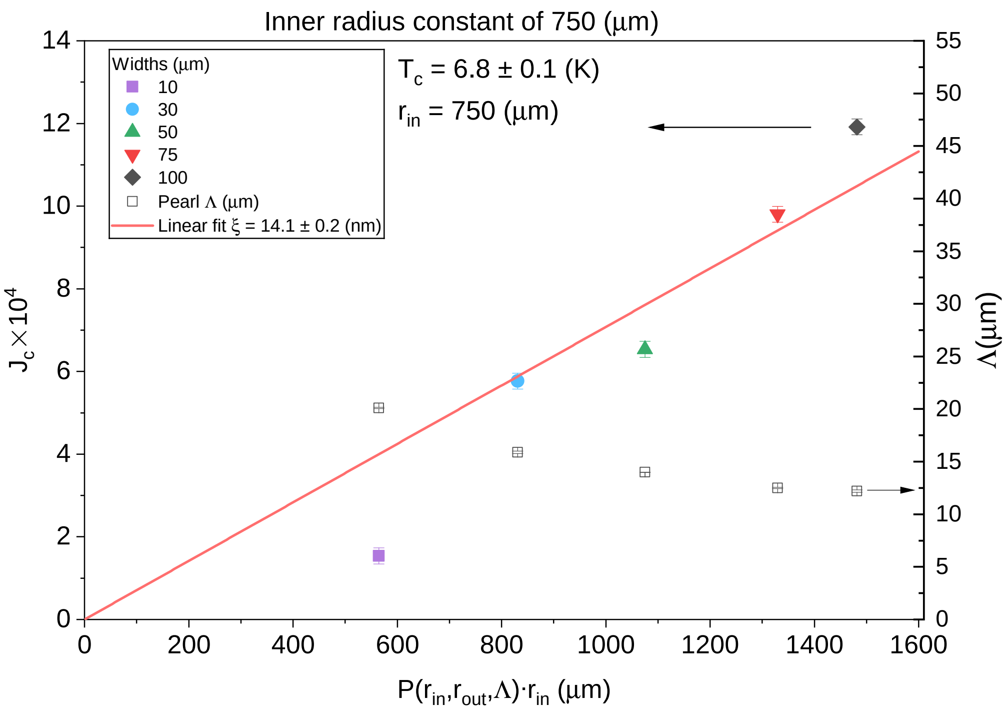

Figure 5.7: Critical flux number, J_c, as a function of the inner radius multiplied by the geometric factor $P(r_{in}, r_{out}, \Lambda) \cdot r_{in}$ as defined in Equation 1.57. Solid data points correspond to the left axis and show measurements for multiple rings with a constant inner radius $r_{in} = 750$ μm and varying widths. The inverse of the slope from the linear fit yields a coherence length of $\xi = 14.1 \pm 0.2$ nm. Hollow data points correspond to the right axis and represent the calculated Pearl length, Λ, for each ring.

Figure 5.5. The table presents the coherence length ξ obtained for each ring, together with the corresponding Pearl length Λ. Since each ring has a different value of Λ, the table emphasizes the influence of both Λ and the ring width on the extracted value of ξ. These variations provide a possible explanation for the deviations of individual data points from the overall linear fit. The results for the rings with widths of 100, 75, and 50 μm shown in Figure 5.5 were obtained from the same sample, which was progressively trimmed from 100 μm to 50 μm. This set gave the most consistent values of Λ. In contrast, samples fabricated in the same sputtering batch still showed variations in their parameters, including the critical temperature, Pearl length Λ, and the extracted coherence length ξ.

Table 5.1: Summary of the extracted coherence length ξ values and relevant geometric and physical parameters for all measured rings. The top section presents samples with a constant outer radius $r_{out} = 800$ μm, while the bottom section details samples with a constant inner radius $r_{in} = 750$ μm. Tabulated values include the inner and outer radii r_{in}, r_{out}, track width, calculated Pearl length Λ, geometric scaling factor P, measured critical flux number J_c, and the resulting ξ.

r_{in} [μm]±2	r_{out} [μm]±2	*Width* [μm]	Λ [μm]	$P \pm 0.03$	J_{c}±$0.1 \cdot 10^4$	ξ [nm]
790	800	10	85±0.3	0.61	2.7	18.1 ± 1.5
750	800	50	74±0.14	0.73	3.7	15 ± 1
725	800	75	69.8±0.2	0.79	4.0	14.7 ± 0.9
700	800	100	70.3±0.2	0.86	4.4	14.1 ± 0.8
750	760	10	20.1 ±0.06	0.75	1.5	36 ± 5
750	780	30	15.89±0.04	1.10	5.6	14.4 ± 0.5
750	800	50	13.99±0.03	1.43	6.5	16.4 ± 0.6
750	825	75	12.5±0.02	1.77	9.8	13.5 ± 0.4
750	850	100	12.2±0.02	1.97	11.91	12.4 ± 0.3

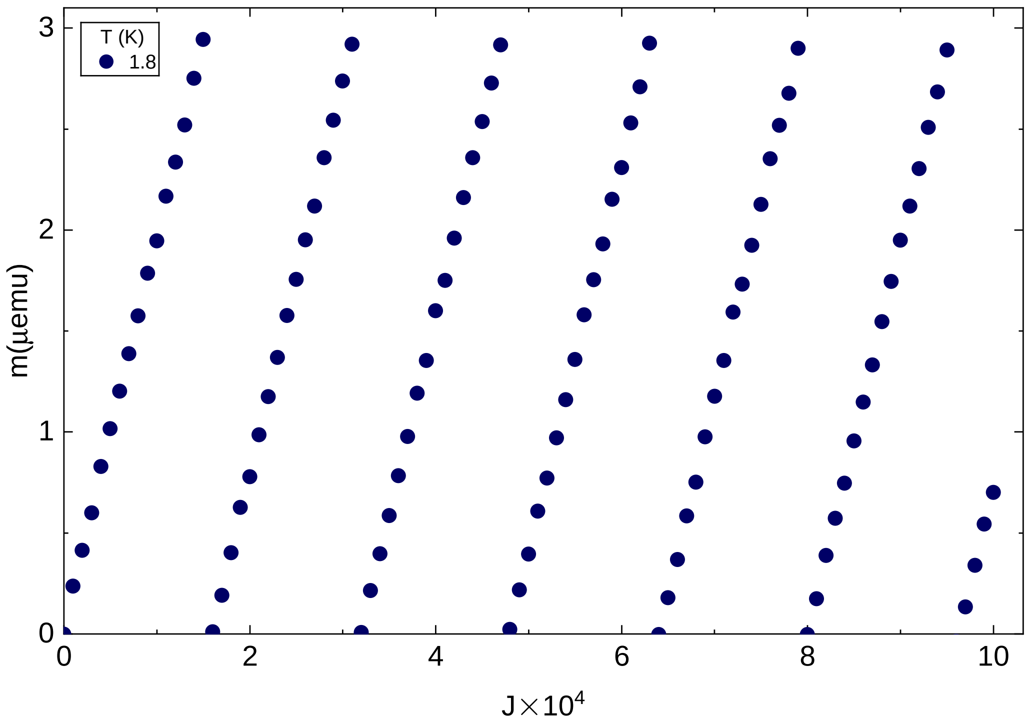

Figure 5.8: Magnetic response as a function of excitation coil flux number for a thin and narrow ring with a width of 10 μm and $r_{in} = 750$ μm. The measurement was performed at 1.8 K.

5.2 Multiple flux jumps

Some of the samples exhibited sharp jumps in the magnetic moment as the applied flux was increased. Figure 5.8 shows these jumps, as well as their periodicity, with jumps occurring approximately every $J = 1.4 \cdot 10^4$. The magnetic moment reaches nearly the same value before each jump, and the spacing between successive jumps remains approximately constant.

When the critical magnetic moment, approximately 3 μemu, is reached, the moment drops close to zero. This indicates that the superconducting current in the ring is strongly suppressed after the jump. In this state, the vector potential induced by the excitation coil is effectively compensated by the phase-gradient term, $\nabla\phi$, in the ring.

Although the samples were fabricated from the same target and deposition batch, this behavior was not universally observed across all rings. To verify the response, the measurements were repeated using negative applied flux, thereby reversing the direction of the induced vector potential. As illustrated in Figure 5.9, this symmetric behavior was also present in a wider ring with a track width of 100 μm.

To further characterize this ring, the magnetic response was measured across a range of temperatures. The results indicate that the jump periodicity is temperature-dependent, scaling directly with the temperature dependence of the critical magnetic moment. As demonstrated in Figure 5.10, only a single jump occurs within the measured flux range at 1.8 K, whereas three distinct jumps are visible at 4.8 K.

According to Equation 1.72, the recovery time of the order-parameter amplitude, ψ, in our

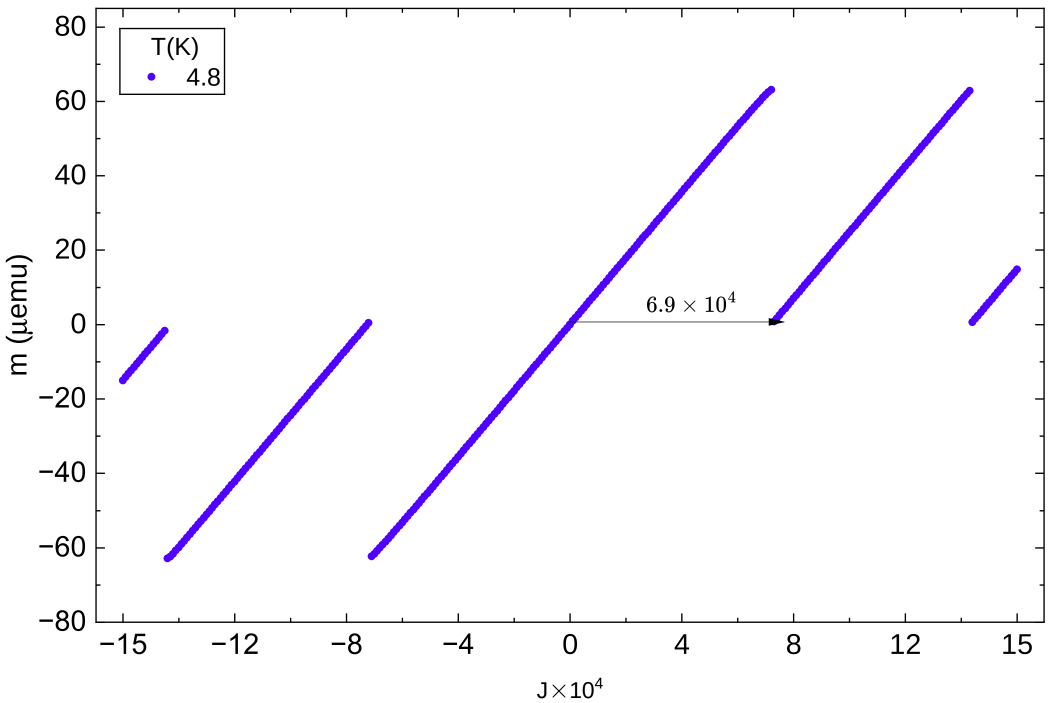

Figure 5.9: Magnetic response as a function of excitation coil flux number for positive and negative flux in a thin, narrow ring with a width of 100 μm and r_{in} = 750 μm, measured at 4.8 K.

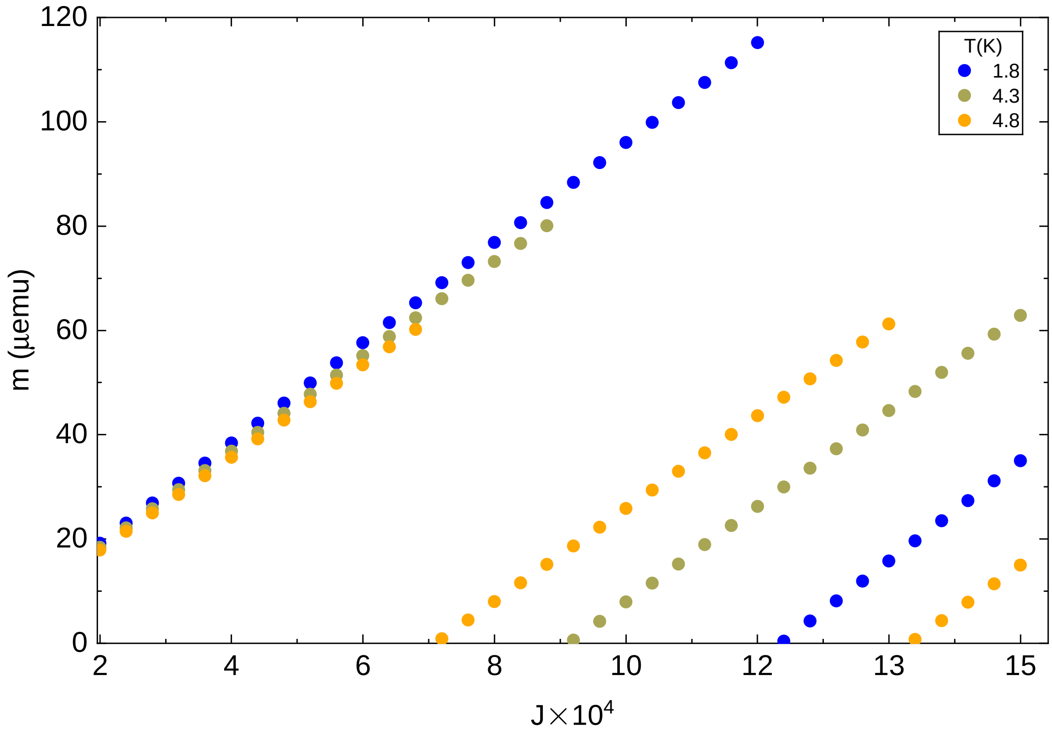

Figure 5.10: Magnetic response as a function of excitation coil flux number. The measurement was performed on a ring with width of 100 μm and r_{in} = 750 μm, measured at different temperatures.

rings is much longer than the recovery time of the superconducting phase, ϕ [12, 7]. Therefore, when the ring reaches the critical magnetic moment, the phase gradient, $\nabla\phi$, can adjust much faster than the amplitude can recover. This rapid phase adjustment may trigger a cascade of phase-slip events [22, 8], in which the winding number of the superconducting order parameter changes and additional flux enters the ring in discrete units of the flux quantum, Φ_0. Each flux quantum introduced reduces the overall magnetic moment. In our measurements, the sharp jumps in the magnetic moment indicate that many flux quanta enter the ring during each event, reducing the magnetic moment nearly to zero. This interpretation is consistent with studies of flux-biased superconducting rings, where phase slips occur near the instability of a metastable fluxoid state and are accompanied by jumps in the persistent current [22, 8]. This behavior differs from that reported in Ref. [7], where multiple-flux jumps do not reduce the magnetic moment to zero, but instead cause it to oscillate around a finite value.

Chapter 6

Conclusions

We present the extraction of the superconducting coherence length, ξ, using a stability based approach based on the theoretical model developed by Rabaglia, Keren, and Turner for our ring geometry [23]. This model can be applied to individual samples, and can also be used to verify ξ by comparing the linear trend obtained from several samples with different geometries. The previous approach, described by Equation 1.70, does not fully capture the behavior of the ring. As shown in Figure 5.4, the critical flux number J_c decreases even when the outer radius is held constant. In contrast, the updated model presented in Equation 1.57 provides a more comprehensive description by explicitly accounting for the ring's inner radius, outer radius, and Pearl length.

For the samples studied, the prefactor Equation 1.57, does not reach the expected asymptotic limit of $1/\sqrt{3}$, of very-narrow-ring. This deviation is a direct consequence of the finite Pearl length, Λ, which is not sufficiently large relative to the ring dimensions to fully justify the very-narrow-ring approximation. Consequently, calculations of P are essential.

Periodic collapses of the magnetic moment as a function of the applied flux are observed for some samples. These jumps reduce the magnetic moment of the sample to approximately zero, indicating that the superconducting current is strongly suppressed during each jump. In addition, the ring width and temperature affect the overall critical magnetic moment, which in turn influences the observed periodicity. At present, we do not have a good explanation for the conditions required for these jumps.

Bibliography

[1] John Bardeen, Leon N. Cooper, and J. Robert Schrieffer. Theory of superconductivity. *Physical Review*, 108(5):1175–1204, 1957.

[2] Michael Tinkham. *Introduction to Superconductivity, 2nd Edition*. McGraw-Hill, 1996.

[3] J. Pearl. Current distribution in superconducting films carrying quantized fluxoids. *Applied Physics Letters*, 5(4):65–66, August 1964.

[4] John David Jackson. *Classical Electrodynamics*. John Wiley & Sons, New York, 3 edition, 1999.

[5] Amit Keren, Nitsan Blau, Nir Gavish, Oded Kenneth, Yachin Ivry, and Mohammad Suleiman. Stiffness and coherence length measurements of ultra-thin superconductors, and implications for layered superconductors. *Superconductor Science and Technology*, 35(7):075013, jun 2022.

[6] Nir Gavish, Oded Kenneth, and Amit Keren. Ginzburg–landau model of a stiffnessometer — a superconducting stiffness meter device. *Physica D: Nonlinear Phenomena*, 415:132767, 2021.

[7] D. Y. Vodolazov, F. M. Peeters, S. V. Dubonos, and A. K. Geim. Multiple flux jumps and irreversible behavior of thin Al superconducting rings. *Physical Review B*, 67(5):054506, February 2003.

[8] I. Petković, A. Lollo, L. I. Glazman, and J. G. E. Harris. Deterministic phase slips in mesoscopic superconducting rings. *Nature Communications*, 7:13551, 2016.

[9] D. Y. Vodolazov and F. M. Peeters. Dynamic transitions between metastable states in a superconducting ring. *Physical Review B*, 66(5):054537, 2002.

[10] D. E. McCumber and B. I. Halperin. Time scale of intrinsic resistive fluctuations in thin superconducting wires. *Physical Review B*, 1(3):1054–1070, 1970.

[11] C. J. Olson, C. Reichhardt, and Franco Nori. Superconducting vortex avalanches, voltage bursts, and vortex plastic flow: Effect of the microscopic pinning landscape on the macroscopic properties. *Physical Review B*, 56(10):6175–6194, 1997.

[12] B. J. Baelus, F. M. Peeters, and V. A. Schweigert. Vortex states in superconducting rings. *Physical Review B*, 61(14):9734–9747, 2000.

[13] H. Polshyn, T. R. Naibert, and R. Budakian. Imaging phase slip dynamics in micron-size superconducting rings. *Physical Review B*, 97(18):184501, 2018.

[14] Itay Mangel, Itzik Kapon, Nitzan Blau, Katrine Golubkov, Nir Gavish, and Amit Keren. Stiffnessometer: A magnetic-field-free superconducting stiffness meter and its application. *Phys. Rev. B*, 102:024502, Jul 2020.

[15] Amotz Peri, Itay Mangel, and Amit Keren. Superconducting stiffness and coherence length of fese$_{0.5}$te$_{0.5}$ measured in a zero-applied field. *Condensed Matter*, 8(2), 2023.

[16] Shugo Kubo. Superconducting properties of amorphous MoX (X = Si, Ge) alloy films for abrikosov vortex memory. *Journal of Applied Physics*, 63(6):2033–2045, 1988.

[17] D. Bosworth, S.-L. Sahonta, R. H. Hadfield, and Z. H. Barber. Amorphous molybdenum silicon superconducting thin films. *AIP Advances*, 5(8):087106, 2015.

[18] Xiaofu Zhang, Ilya Charaev, Huanlong Liu, Tony X. Zhou, Dong Zhu, Karl K. Berggren, and Andreas Schilling. Physical properties of amorphous molybdenum silicide films for single-photon detectors. *Superconductor Science and Technology*, 34(9):095003, 2021.

[19] L. Ceccarelli, D. Vasyukov, M. Wyss, G. Romagnoli, N. Rossi, L. Moser, and M. Poggio. Imaging pinning and expulsion of individual superconducting vortices in amorphous MoSi thin films. *Physical Review B*, 100(10):104504, 2019.

[20] Quantum Design. *MPMS 3 User's Manual*. Quantum Design. Revision F4.

[21] F. Hecht. New development in freefem++. *J. Numer. Math.*, 20(3-4):251–265, 2012.

[22] I. Petkovic, A. Lollo, and J. G. E. Harris. Phase-slip statistics of a single isolated flux-biased superconducting ring. *Physical Review Letters*, 125:067002, 2020.

[23] R. Rabaglia, A. Keren, and A. Turner. Vortex penetration and instability of Aharonov–Bohm-driven supercurrents in thin superconducting rings. In preparation.

הוא זה שנשמר קבוע בעוד שהרדיוס החיצוני שונה בהדרגה, אותו ניתוח הוביל לערך המובהק $\xi = 14.1 \pm 0.2$ nm. רמת העקביות הגבוהה והחפיפה המרשימה בין שני הערכים שהופקו, על אף השונות הגיאומטרית הניכרת בין שתי סדרות הדגמים, מספקת אישוש פיזיקלי רב-עוצמה לאמינות המודל התיאורטי החדש המשלב את מודל הפלוקטואציות. עקביות מוכחת זו סוללת למעשה את הדרך לביצוע מדידות אמינות, הדירות ומדויקות ביותר של סקלות האורך היסודיות גם בשורה ארוכה של חומרים מוליכי-על עתידיים, תוך הבטחת דיוק רב מאי-פעם. מעבר למדידות הסטטיות ולבחינת סקלות האורך, מהלך המחקר המעשי חשף תופעה דינמית ומפתיעה הנוגעת לאופי הלא-ליניארי של מוליכי-העל במימדים אלו. בחלק ניכר מהדגמים הפיזיקליים שנבחנו, הבחנו בקפיצות חדות, מהירות ומחזוריות ביותר בערכו של המומנט המגנטי של הטבעת. תופעה זו התרחשה ככל שהפוטנציאל הווקטורי המגנטי החיצוני הוגדל בהדרגה על ידי השדה המופעל. קפיצות פתאומיות אלו גרמו לצניחה כמעט מיידית של המומנט המגנטי הנמדד אל קרוב לערך אפס, צניחה המעידה באופן מובהק על דיכוי חזק ורגעי של זרם-העל העובר בטבעת במהלך כל מעבר כזה. בניתוח התופעה התברר כי מחזוריות הקפיצות הללו לא הייתה אקראית, אלא הראתה תלות שיטתית וברורה בטמפרטורת המדידה ובגיאומטריה המדויקת של כל טבעת. תלות זו מרמזת בצורה משמעותית כי אי-היציבות המובילה לאותן קפיצות קשורה באופן הדוק לשינויים טופולוגיים בפאזה של פונקציית הגל המקרוסקופית. תהליך זה משקף למעשה מעברים דינמיים בין מצבים מטא-יציבים נושאי-זרם, שבהם המערכת משחררת או קולטת קוואנטים של שטף כדי להגיע למצב יציב מבחינה אנרגטית. לסיכום העבודה, מחקר זה מדגים בפועל את היעילות והפוטנציאל הגלומים בשימוש במערכות מדידה מבוססות מד-קשיחות לשם חילוץ סקלות אורך קריטיות בטבעות דקות מוליכות-על. בנוסף, התזה מדגישה מעל לכל ספק את החשיבות העליונה של התחשבות בהשפעות גיאומטריות ואפקטים של סיכוך מגנטי כחלק בלתי נפרד מפענוח התגובה הקריטית של טבעות על-מוליכות, ממצאים העשויים לשמש בעתיד אבן יסוד לתכנון ופיתוח של התקנים ננו-אלקטרוניים מתקדמים.

תקציר

מוליכות-על היא תופעה קוונטית מקרוסקופית מרתקת, אשר מתאפיינת בשתי תכונות פיזיקליות יסודיות המתרחשות כאשר חומר מסוים מקורר אל מתחת לטמפרטורה קריטית ייעודית. התכונה הראשונה היא הולכה חשמלית מושלמת ללא כל התנגדות, המאפשרת מעבר זרם ללא פיזור אנרגיה, והתכונה השנייה היא דחייה מוחלטת של שטפי שדה מגנטי מתוך גוף החומר, המוכרת כאפקט מייסנר. בתזה זו, מוקד המחקר הוא הבנת ההתנהגות הפיזיקלית במבנים ננומטריים, ובפרט בטבעות מוליכות-על דקות וצרות. גיאומטריה ייחודית זו מאפשרת לבחון לעומק את האופי הקוונטי של החומר תחת אילוצים מרחביים קפדניים. המחקר המובא כאן נשען על שימוש במערכת מתקדמת למדידות קשיחות (Stiffnessometer), שמטרתה לבחון בדיוק חסר תקדים את התגובה האלקטרודינמית של הקונדנסט העל-מוליך למגוון רחב של פוטנציאלים וקטוריים מגנטיים. יעד מרכזי של עבודה זו הוא לכמת ולהגדיר במדויק את סקלות האורך הפיזיקליות הרלוונטיות הקובעות את התנהגות המערכת: עומק החדירה של לונדון λ, המתאר את דעיכת השדה המגנטי בתוך החומר, אורך פרל Λ, המהווה סקלת אורך אפקטיבית החיונית להבנת תהליכי מיסוך מגנטי במערכות של סרטים דקים ודו-ממדיים, ואורך הקוהרנטיות של מוליך-העל ξ, המייצג את המרחק האופייני שבו פונקציית הגל המקרוסקופית, או פרמטר הסדר, שומרת על יציבותה ומשתנה במרחב מבלי לקרוס. ההבנה המדויקת של גדלים אלו היא קריטית לפיתוח מודלים נכונים של מוליכות-על בממדים קטנים. בעבודות מחקר קודמות שבוצעו במסגרת קבוצתנו, ההערכה של אורך הקוהרנטיות ξ התבססה על גישה תיאורטית של קירוב שדה ממוצע. על פי גישה מסורתית זו, השטף המגנטי הקריטי – כלומר, כמות השטף המקסימלית שהטבעת מסוגלת לשאת בטרם מצב מוליכות-העל קורס לחלוטין – תלוי כמעט באופן בלעדי בהרס המשרעת של פרמטר הסדר. בהתבסס על הנחה זו, המסקנה הנגזרת הייתה כי הרדיוס החיצוני של הטבעת העל-מוליכה מהווה את הפרמטר הגיאומטרי המכריע והדומיננטי ביותר בקביעת גבולות היציבות של המערכת כולה. עם זאת, במסגרת עבודת תזה זו, אני מראה בצורה חד-משמעית כי הקירוב הקלאסי של שדה ממוצע איננו מספיק כדי ללכוד את התמונה הפיזיקלית המלאה והמורכבת של התופעה. מתברר כי כדי להבין באמת את מנגנוני הקריסה של זרם-העל בטבעות דקות, הכרחי לקחת בחשבון את יציבות הפתרון התיאורטי באמצעות בחינה מתמטית קפדנית של פלוקטואציות תרמיות וקוונטיות, המערערות את המערכת לאורך זמן. כאשר משלבים את השפעתן של הפלוקטואציות הללו למודל, מתקבלת תוצאה מפתיעה המשנה את הפרדיגמה הקודמת: דווקא הרדיוס הפנימי של הטבעת הוא זה שתופס את התפקיד המרכזי והמשמעותי ביותר בשמירה על יציבות המערכת או בקריסתה. יתרה מזאת, המחקר מדגיש כי השטף המגנטי הקריטי בפועל איננו נשען על פרמטר גיאומטרי מבודד, אלא נקבע על ידי השילוב של הגיאומטריה המרחבית השלמה של הטבעת. קיימת אינטראקציה עמוקה בין הרדיוס הפנימי לרדיוס החיצוני, ואלו תלויים לחלוטין בהשפעתו של אורך פרל המכתיב את התנהגות המיסוך בשכבות דקות. על מנת לאמת ולהוכיח את הגישה התיאורטית המעודכנת הזו, עשיתי שימוש ניסויי מקיף בערכי השטף הקריטי כפי שנמדדו הלכה למעשה במערכת המדידה, בטמפרטורות משתנות ובתנאי סביבה מבוקרים. על ידי שילוב של הנתונים האמפיריים המדויקים הללו יחד עם הפיתוחים התיאורטיים האחרונים, הצלחתי לחלץ ולהגדיר את ערכו המדויק של אורך הקוהרנטיות ξ עבור שתי סדרות נפרדות של טבעות ננומטריות שיוצרו מסגסוגת מוליכת-על של מוליבדנום-סיליסייד (MoSi). סדרות הטבעות הללו תוכננו במיוחד כדי לבודד את המשתנים הגיאומטריים ולבחון את השפעתם באופן בלתי תלוי. בסדרת הטבעות הראשונה, שבה הרדיוס החיצוני נשמר קבוע בעוד שהרדיוס הפנימי עבר שינויים מבוקרים מדגם לדגם, תהליך ניתוח הנתונים המדוקדק הניב את הערך $\xi = 15.2 \pm 0.5$ nm. לעומת זאת, עבור סדרת הטבעות השנייה, שבה ננקטה גישה הפוכה והרדיוס הפנימי

המחקר נעשה בפקולטה לפיזיקה בהנחיית פרופסור קרן עמית. מחבר חיבור זה מצהיר כי המחקר, כולל איסוף הנתונים, עיבודם והצגתם, התייחסות והשוואה למחקרים קודמים וכו', נעשה כולו בצורה ישרה, כמצופה ממחקר מדעי המבוצע לפי אמות המידה האתיות של העולם האקדמי. כמו כן, הדיווח על המחקר ותוצאותיו בחיבור זה נעשה בצורה ישרה ומלאה, לפי אותן אמות מידה.

הכרת תודה מסורה לטכניון על מימון מחקר זה.

מדידת קשיחות של טבעות על מוליכות דקות וצרות

חיבור על מחקר

לשם מילוי חלקי של הדרישות לקבלת התואר
מגיסטר למדעים בפיזיקה

עומרי טאבו

הוגש לסנט הטכניון — מכון טכנולוגי לישראל
אב התשפ"ו חיפה אוגוסט 2026

מדידת קשיחות של טבעות על מוליכות דקות וצרות

עומרי טאבו